Model Analysis of Edge Relaxation Phenomena in Tokamak Plasmas

MATSUKAWA, Shogo
Interdisciplinary Graduate School of Engineering Sciences, Kyushu University

ITOH, Sanae-I.
Research Institute for Applied Mechanics, Kyushu University

YAGI, Masatoshi
Research Institute for Applied Mechanics, Kyushu University

https://doi.org/10.15017/6767929

出版情報：九州大学応用力学研究所所報. 119, pp.39-60, 2000-09. Research Institute for Applied Mechanics, Kyushu University
バージョン：
権利関係：

Model Analysis of Edge Relaxation Phenomena in Tokamak Plasmas

Shogo MATSUKAWA *1, Sanae -I. ITOH *2and Masatoshi YAGI*2

E-mail of corresponding author: *shogo@post.riam.kyushu-u.ac.jp*

(Received April 1, 2000)

Abstract

From the view point of the oscillatory characteristics, the heat transport in the plasma edge region is investigated based on a transition transport model with hysteresis nature. A hysteresis type flux-force relation is incorporated into the model by introducing a transition model of the heat diffusivity. For a given influx from the upstream side, the one dimensional heat transport equation is solved numerically. The time evolution of the heat flux oscillation due to the hysteresis nature and the parameter dependences of its amplitude and frequency are examined. The non-monotonous relation between the frequency of the flux oscillation and the influx is obtained. The critical behavior of the transition between two transport mechanisms, i.e., the hysteresis type and the discontinuous one, is expressed as power law relations of them. The self-organized criticality like bahavior, i.e., power spectrum obeying power law, is found in a limiting case of the model.

Key words : *edge relaxation phenomena, edge localized mode, bifurcation, transition, hysteresis, oscillatory characteristics, self-organized criticality*

1. Introduction

Research on the controlled thermonuclear fusion is an important issue as a candidate for a new energy source in the next generation, and has long been a world wide project. In various kinds of magnetic confinement devices, the tokamak has been most extensively investigated and advanced. Large tokamaks such as JET and JT-60U are making remarkable progress toward a realization of fusion conditions in a confined plasma. Recently, JET has produced slightly in excess of 12MW of fusion power using a D-T plasma.

However, many problems to be solved for the realization of the fusion reactor are still left. For examples, the physical mechanisms of the anomalous transport phenomena or collapse events in high temperature plasmas are needed to be clarified. These phenomena lead to the strong degradation of plasma confinement performance to attain the D-T reaction. It is just recently to reach the boundary of the break even in tokamaks. This is because the anomalous transport causes the degradation of the energy confinement, so-called low confinement mode (L-mode). In the L-mode, it is known empirically that the larger input power leads to the lower plasma confinement. One promising scenario in the tokamak reactor is the operation in the improved confinement regime known as high confinement mode (H-mode). It occurs spontaneously when the heating power exceeds a certain threshold value. Then, the pressure gradient increases near the plasma edge, namely, a transport barrier is formed. However, the bursts of edge localized modes (ELMs), one of collapse events, are frequently observed during the H-mode phase in experiments. The ELMs are characterized by the sudden drop of the plasma pressure with a burst of particle and/or heat flux and lead to a losts of the plasma energy.

In high temperature plasmas in toroidal devices, various kinds of collapse events have been observed [1, 2]. The sawtooth crash [3], the internal disruption [4] and the high-β collapse [5] are examples of collapse events observed in the plasma core region. In the plasma edge region, the bursts of the ELMs are frequently observed during the H-mode phase. The ELMs are categorized at least into three types, i.e., type I, type III and dithers [6]. The type I ELMs, also called the giant ELMs, is observed near the threshold value of β-limit at the plasma surface [7, 8]. Under its occurrence, the pressure repeats the cycles characterized by a slow rise by the heating and a rapid ($10 \sim 100\mu$sec) drop, by which the energy of plasmas is lost periodically or intermittently. The dithering ELMs is the repetitive L-H-L transitions in

*1 Interdisciplinary Graduate School of Engineering Sciences, Kyushu University
*2 Research Institute for Applied Mechanics, Kyushu University

the vicinity of L/H transition condition.

In theoretical works, various kinds of models have been proposed to describe collapse events [9]. The basic models of collapse events can be divided into two categories: the models based on magnetohydrodynamic (MHD) instabilities and the models based on nonlinear transport with limit cycle solution, i.e., hysteresis nature. A simulation of the burst of type-I ELMs has been done assuming that it occurs due to a short breakdown of the transport barrier [10]. Termination of the transport barrier has usually been discussed based on linear MHD stability. It has been reported that the achievable pressure gradient in the H-mode is bounded by the MHD stability [7, 11, 12]. However, the conventional argument has great difficulty in explaining the sudden increase in magnetic fluctuation where the timescale is of the order of 10μsec. The linear MHD mode growth is dictated by the background plasma parameters, whose change only takes place on the slow transport timescale. Recently, a new nonlinear transition transport model has been proposed to explain the collapse events accompanied with the rapid growth of the magnetic fluctuation, such as the giant ELMs or the sawtooth crash [13]. This model is based on the transition from the electrostatic turbulence, which is relevant to explain the L-mode and the H-mode transport, to the electromagnetic turbulence with the braided magnetic field. When the pressure gradient exceeds a certain threshold value, the overlap of the small scale magnetic island occurs and causes the stronger turbulence. By this, the heat diffusivity is enhanced and kept until the pressure gradient falls to another threshold value. In other words, the heat diffusivity has hysteresis nature with respect to the pressure gradient. Such hysteresis nature has a potentiality to explain the fast growth of the outward heat flux and the evacuation of the plasma energy. Employing this hysteresis type transition model, the collapse of the temperature profile and the associated energy burst have been reproduced by simulation study as has been observed in experiments [14, 15]. The role of the hysteresis nature has also been predicted for the dithering ELMs. A model for the dithering ELMs, i.e., the self generated oscillation due to the hysteresis characteristics of the L-H transition, was proposed based on electric field bifurcation theory. This model has shown an agreement with experimental observation on dithering ELMs through simulation study [16]. Among various theoretical models, the transition transport model with hysteresis nature is considered as one of strong candidates for the physical mechanism of the collapse. However, the physical mechanism of the collapse is not yet fully clarified.

In this paper, based on the transition transport model with hysteresis nature, we study the edge relaxation phenomena in high temperature plasmas from the view point of the oscillatory characteristics of the heat transport. The aim of this paper is not to reproduce the collapse, but to examine the transition model with hysteresis nature as one of candidates for the physical mechanism of the collapse. The characteristics of the oscillatory behavior caused by the hysteresis nature are numerically analyzed. To elucidate the dynamics due to the hysteresis nature, a simplified transition model is employed and examined.

This paper is organized as follows. In Chapter 2., the edge relaxation phenomena and the transition models with hysteresis nature are reviewed. In Chapter 3., the simulation model including the transition model with the hysteresis nature is introduced. In Chapter 4., the time evolution and the oscillatory characteristics of the heat transport are analyzed by numerical simulation. In Chapter 5., summary and discussion are given.

2. Reviews

In high temperature plasmas in toroidal devices, various kinds of collapse events have been observed. The edge localized modes (ELMs) are typical examples of collapse events observed in the plasma edge region. To explain the collapse, many theoretical models have been proposed, and simulations based on them have been carried out. However, the physical mechanism of the collapse is not yet fully understood. Among various theoretical models, the transition transport with hysteresis nature is considered as one of strong candidates for the physical mechanism of the collapse.

In this chapter, we firstly review the empirical phenomenology of the ELMs. Next, we show the theoretical models for the ELMs, especially, the transition models with hysteresis nature.

2.1 Edge Localized Modes

Toroidal plasmas are subjected to various kinds of catastrophic phenomena. The achievable plasma parameters have been limited by the occurrence of catastrophic events in addition to the competition between the losses and the external sources. Therefore, the crash phenomena in high temperature plasmas have been considered to be the essential problem in fusion research and is also an academic problem of nonlinear and far-nonequilibrium systems. The characteristics of the collapse events include the typical features as follows: (i) the sudden onset of symmetry-breaking perturbation, (ii) bursts of plasma energy, momentum and particles across magnetic surfaces, (iii) avalanches, i.e., the propagation of the collapses and (iv) the possible periodic occurrences of bursts, and also their unpredictability.

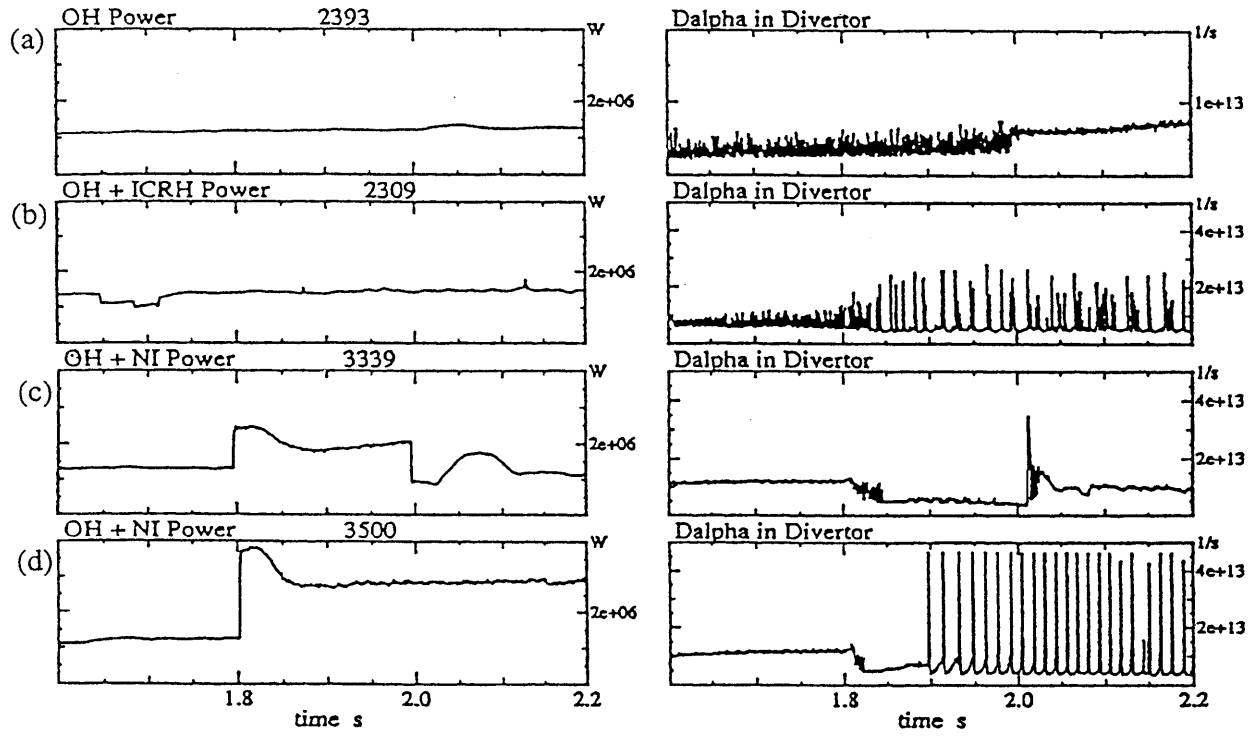

Fig. 1 Comparison of the different dynamic behavior of the H-mode with varying $(P - P_{sep}^{LH})/P_{sep}^{LH}$. (a) $(P-P_{sep}^{LH})/P_{sep}^{LH} \approx 0.0$, (b) $(P-P_{sep}^{LH})/P_{sep}^{LH} \approx 0.2$, (c) $(P-P_{sep}^{LH})/P_{sep}^{LH} \approx 0.5$, (d) $(P-P_{sep}^{LH})/P_{sep}^{LH} \approx 1.2$. (Cited from Ref. [17])

In high temperature plasmas, various kinds of collapse events have been identified [1]. The sawtooth crash [3], the internal disruption [4] and the high-β collapse [5] are examples of collapse events observed in the plasma core region. As typical examples observed in the plasma edge region, the bursts of the edge localized modes (ELMs) are frequently observed during the high confinement mode (H-mode) [6].

The improved confinement mode known as H-mode is often perturbed by the onset of a quasi-periodic series of relaxation oscillations involving bursts of MHD activity and D_α emission, known as ELMs. These result in rapid losses of particles and energy from the region near the plasma boundary, reducing the average global energy confinement by 10 $\sim$ 20%. Furthermore, these transient bursts of energy and particles into the scrape-off layer produce high peak heat loads on the divertor plates which must be accommodated by the divertor design. On the other hand, ELMs are more efficient, and beneficial, in removing density and impurities. Thus they are deemed necessary for the stationary H-mode operation, preventing the build-up of density, impurities and helium ash. It is, therefore, desirable to be able to control the level and nature of the ELM activity in order to meet these various conflicting conditions. This would be aided by understanding their cause.

The characterization of ELMs has recently began. For example, the classification of ELMs in ASDEX-Upgrade experiments was made [17]. At the heating power near the threshold power for the L-H transition, a self generated oscillation of periodic L-H-L transition occurs. For $(P - P_{sep}^{LH})/P_{sep}^{LH} > 0.2$, ELMs called type III occur, where P is the injected power and P_{sep}^{LH} is the threshold power value of the L/H transition. They are characterized by $d\nu_{ELM}/dP < 0$, where ν_{ELM} is the frequency of ELMs. The frequency decreases as the power is increased. For $(P - P_{sep}^{LH})/P_{sep}^{LH} \geq 0.5$, the discharge becomes ELM-free. ELMs called type I occur for $(P - P_{sep}^{LH})/P_{sep}^{LH} \geq 1$. They are characterized by $d\nu_{ELM}/dP > 0$. The power dependence of the type I ELM frequency is opposite to that of type III. These ELMs are considered to appear when the edge plasma parameter is close to the critical value of the ideal MHD mode stability [7, 11, 18, 19]. Comparison of the different dynamic behavior of the H-mode with varying $(P - P_{sep}^{LH})/P_{sep}^{LH}$ is shown in Fig 1.

The new classification has been done, taking the experimental results in the other toroidal fusion devices

into account in addition to ASDEX-Upgrade's [6]. ELMs are classified into the three distinct types according to the occurrence of the magnetic precursor and the dependence of the ELM frequency on the energy flux through the separatrix, P_{sep}. The distinct types of the ELMs are as follows.

- Type I ELMs (giant ELMs): The burst occurs near the ideal ballooning limit $\alpha \approx \alpha_{crit}$. The ELM repetition frequency ν_{ELM} increases with the energy flux through the separatrix P_{sep}, rather than the injected power P, i.e.,

$$\frac{d\nu_{ELM}}{dP_{sep}} > 0. \quad (1)$$

  In present experimental results, no clear magnetic precursor oscillation has been identified. During the ELM, there is a high level of incoherent magnetic fluctuations.

- Type III ELMs: At $P_{sep} \approx P_{sep}^{LH}$, heating powers just above the threshold for L-H transition, the bursts of type III ELMs occur. The ELM cycle frequency decreases with the power through the separatrix, i.e.,

$$\frac{d\nu_{ELM}}{dP_{sep}} < 0. \quad (2)$$

  There is a coherent magnetic precursor oscillation with toroidal mode number $n \approx 5 \sim 10$ and poloidal mode number $m \approx 10 \sim 15$ on the magnetic probes located close to plasma, especially in the outboard midplane. During the ELM, a high level of magnetic fluctuations has been detected.

- Dithering ELMs: At $P_{sep} \approx P_{sep}^{LH}$, prior to the final transition to H-mode, repetitive L-H-L transitions can occur. The repetition frequency shows a slight decrease with increasing P_{sep}. The dithering cycles does not show the MHD signatures as found in type III ELMs: there is no magnetic precursor oscillation, and the level of turbulence during the temporary L-phase does not significantly exceed that of the L-phase at $P_{sep} \leq P_{sep}^{LH}$.

Figure 2 shows the input power and the D_α signal at the divertor for the typical sequence of ELMs during a power rise in DIII-D. Here, D_α signal represents the energy flux from the plasma surface. In a discharge where the heating power is increased in step, type III ELMs occur at heating power just above the threshold for L-H transition P_{sep}^{LH}. Their frequency decreases as P increases until finally they are stabilized and an ELM-free phase appears. With a further rise in the heating power, type I ELMs (giant ELMs) occur at even higher P, their frequency now increases with P, although it decreases with plasma current I. Then, the time scale of the crash becomes the order of 10μsec.

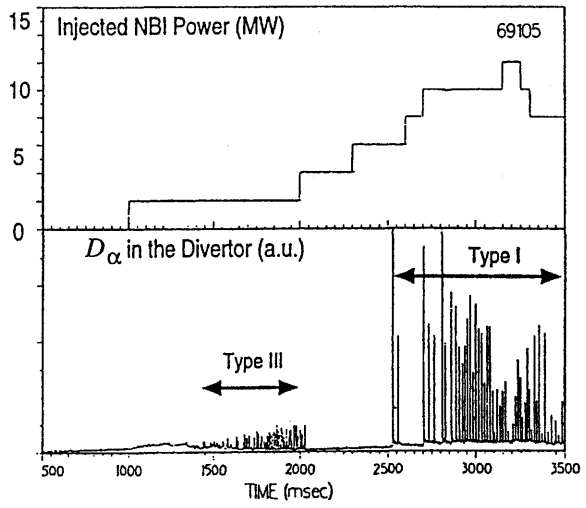

Fig. 2 Typical sequence of ELMs during a power rise in DIII-D. At $P \approx P_{sep}^{LH}$, type III ELMs are found. At higher P, type I ELMs (giant ELMs) occur. (Cited from Fig.2 in Ref. [6])

The different types of ELM have different effects on the plasma. Type I ELMs change the energy content W by $\delta W \leq 10\%$ and δW is rather independent of P but decreases with increasing I. For type III ELMs, $\delta W \approx 1 \sim 5\%$.

Because of the observations of magnetic fluctuations associated with ELMs it is interesting to relate the edge pressure gradients to the critical values for ideal ballooning stability. Type III ELMs occur when the normalized pressure gradient α lies below the critical value for ideal instability, α_{crit}, so the ideal modes can be excluded as an explanation for them, although resistive ballooning modes may be involved. Indeed there is evidence that a critical edge temperature exists above which type III ELMs disappear. For type I ELMs $\alpha/\alpha_{crit} \simeq 1$ and the ideal ballooning modes can be expected to play a role.

2.2 Transition Models with Hysteresis Nature

The theoretical models of ELMs can be divided into three categories: two basic models, i.e., a model based on magnetohydrodynamic (MHD) instabilities and a model based on nonlinear transport with limit cycle solution, and a model by the combination of these two types.

A class of models is based on MHD stability analysis, which examines whether MHD modes could be unstable at the ELM onset. Since ELMs are accompanied by bursts of magnetic perturbation, a number of models involve the excitation of various MHD instabilities: ideal

and resistive ballooning modes, external kink modes and so-called 'peeling modes' [20]. Such models envisage that the application of auxiliary heating drives the equilibrium to a state which triggers MHD instability, resulting in the loss of plasma, followed by a recovery stage until the cycle is repeated. Detailed MHD stability analyses on experimentally plausible pressure and current profiles have performed to determine whether they are linearly unstable to a specific MHD instability. However, the usual linear stability analysis hardly predicts the effect of the mode on transport. This has to be inferred from the nonlinear stability analysis. The effect of the saturated mode, or the combined effect of several nonlinearly interacting modes, on confinement has to be examined. Such nonlinear MHD stability analysis is usually difficult to compute. Thus, theoretical study of the nonlinear MHD effect on transport has not been given so far. Furthermore, the ELM cycle as the dynamics has often been discussed in a phenomenological manner.

Other models involve limit cycle solutions of the nonlinear transport equations governing the plasma edge region, exploiting the electric bifurcation inherent in theories of the L-H transition. A number of models for the L-H bifurcation mechanisms involving nonambipolar losses and the reduction of anomalous transport due to the radial electric field shear have been proposed. By introducing spatio-temporal variation into these models it is possible to obtain limit-cycle behavior. Such models might describe the sequence of bursts of ELMs. As an example of this type model, we briefly review a model for dithering ELM based on the radial electric field bifurcation theory in subsection 2.2.1.

Finally, elements of both two basic models mentioned above, i.e., MHD stability and nonlinear transport, have been combined, with MHD or pressure driven fluctuation transport playing a role. The MHD stability analyses have really only addressed the question which MHD modes become unstable at the ELM onset, and the ELM cycles in these models were generally no more than phenomenological. The models with limit cycle oscillation have made little connection with MHD although there are the facts that MHD fluctuations are invariably observed. As an example of the model that contains both MHD triggering and cycle mechanisms, the magnetic braiding mode (M-mode) transition model of the giant ELM is reviewed in subsection 2.2.2.

2.2.1 Electric Field Bifurcation

The first theory for the L-H transition was proposed in which the bipolar loss is included in order to obtain the consistent ambipolar radial electric field [21]. A bifurcation in the particle flux associated with the change of the radial electric field is found. In this theory, the particle and energy fluxes can have multiple values for the same parameters of density and temperature. The edge region of plasma column $|a-r| \leq \rho_{pi}$ is attributed to the direct orbital loss region (a: minor radius, $\rho_{pi} \equiv v_{Ti} m_i q R/(aeB_t)$: ion poloidal gyroradius, B_t: toroidal magnetic field). The ion orbital loss was given by

$$\Gamma_i = (n_i \nu_{ii}/\sqrt{\epsilon})\rho_{pi} F, \tag{3}$$

where the coefficient F is proportional to the relative number of particle in the loss cone in the velocity space, $0 < F < 1$ and n_i is the ion density. In order to estimate F in the presence of radial electric field E_r, two simple assumptions were made: (i) The ions which satisfy the resonance condition $v_\parallel/(qR) = E_r/(rB_t)$ are lost directly. (ii) The ion distribution function f_i is close to the Maxwellian, $f_i \propto \exp(-v_\parallel^2/v_{Ti}^2)$. Then the estimation $F \propto \exp\left\{-(\rho_{pi} e E_r/T_i)^2\right\}$ was made and the ion loss has the form

$$\Gamma_i^{lc} = \frac{n_i \nu_{ii} \rho_{pi} \hat{F}}{\sqrt{\epsilon}} \exp\left\{-\left(\frac{e\rho_{pi} E_r}{T_i}\right)^2\right\}, \tag{4}$$

where the coefficient $\hat{F}$ is the contribution of the bounce average. On the other hand, the anomalous loss was taken as

$$\Gamma_{e-i}^{anom} = -D_{e0}^b n_e \left(\frac{n_e'}{n_e} + \alpha \frac{T_e'}{T_e} + \frac{eE_r}{T_e}\right), \tag{5}$$

where α is a numerical coefficient of the order of unity. The parameter D_{e0}^b is the bipolar part of anomalous diffusivity. The prime denotes the derivative with respect to the radial direction. Equating Eqs. (4) and (5), the equation to determine the ambipolar electric field was given as

$$\exp\left\{-\left(\frac{e\rho_{pi} E_r}{T_i}\right)^2\right\} = d_0 \left\{\lambda - \left(\frac{e\rho_{pi} E_r}{T_i}\right)\right\} \equiv \hat{\Gamma}, \tag{6}$$

where $d_0 = D_{e0}^b \sqrt{\epsilon}/(\rho_{pi}^2 \hat{F} \nu_{ii})$ and $\lambda = -\rho_{pi}(n_e'/n_e + \alpha T_e'/T_e)$. Figure 3 (a) illustrates the λ dependence of $\hat{\Gamma}$ as the solution of Eq. (6) and Fig 3 (b) shows the λ dependence of the radial electric field. When λ is below the critical value λ_c, the electric field is negative and the fluxes are large. If λ exceeds λ_c, the electric field turns to be positive and the fluxes are reduced. The L-mode corresponds to the branch of the large loss flux and the H-mode is that of the reduced loss flux. It is shown that the bifurcation from the L- to H-mode takes place as $A \to B' \to C \to C' \to D$ and that from the H- to L-mode occurs at $D \to C' \to B \to B' \to A$. Because λ_c for the L- to H-mode transition is larger than that for the H- to L-mode transition, there is a hysteresis in the relation of $\hat{\Gamma}$ and λ as shown in Fig. 3 (a).

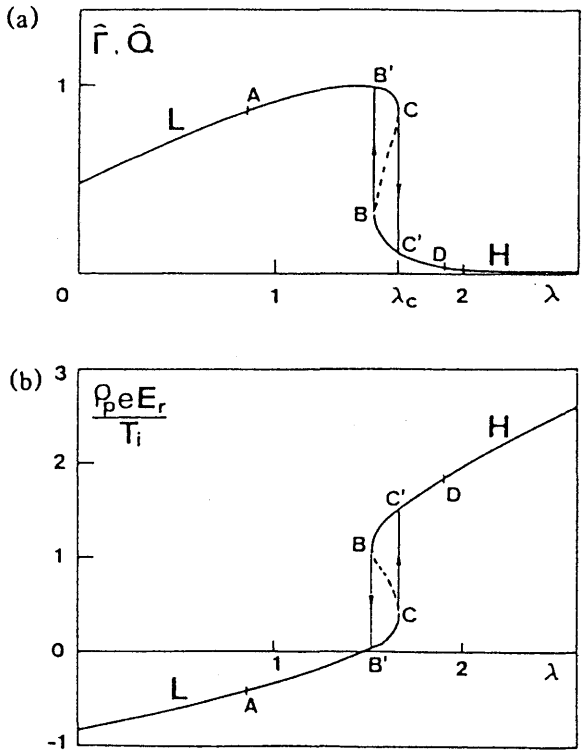

Fig. 3 Solutions for (a) the normalized flux and (b) the radial electric field as a function of λ (for the case of $d_0 = 1.3$). Transition from the branch of the large flux to that of small flux occurs at $\lambda = \lambda_c$. (Cited from Ref. [21])

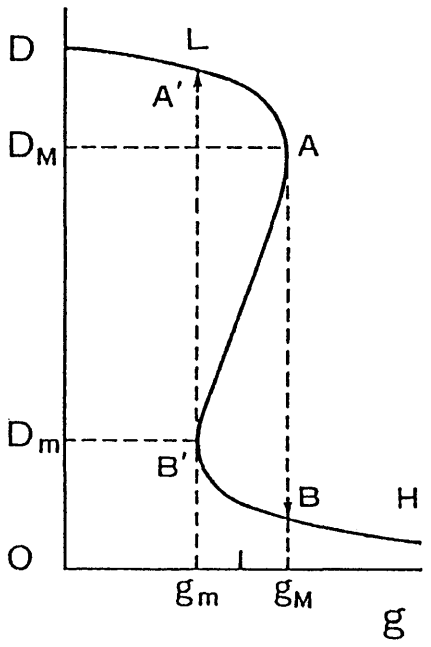

Fig. 4 A model of effective diffusivity D (i.e. ratio of the particle flux to the density gradient) as a function of gradient parameter g, showing the possibility of bifurcations and hysteresis. (Cited from Ref. [22])

A model for the dithering ELM, i.e., the self-generated oscillation due to the hysteresis characteristics of the L-H transition [22], was proposed based on electric field bifurcation theory [21]. The earlier local L-H bifurcation model has been extended by including radial transport equations for the normalized density n and radial electric field Z

$$\frac{\partial n}{\partial t} = \frac{\partial}{\partial x} D(Z) \frac{\partial n}{\partial x} \tag{7}$$

$$\epsilon \frac{\partial Z}{\partial t} = -N(Z, g) + \mu \frac{\partial^2 Z}{\partial x^2} \tag{8}$$

where ϵ is a smallness parameter, and the transport coefficients μ and D are comparable in magnitude $\sim D_0$. N represents the non-ambipolar flux of local theory, $g = \lambda d$ where $\lambda = \rho_{pi}/L_n$ with ρ_{pi} a poloidal ion Larmor radius and L_n the density scale length and $d = D_0/\nu_i \rho_{pi}^2$ where ν_i is the ion collisionality. A model S-curve for N is assumed as

$$N = g - g_0 + \beta(Z^3 - \alpha Z), \tag{9}$$

where $D(Z)$ is a smooth function,

$$D(Z) = \frac{D_{\max} + D_{\min}}{2} + \left(\frac{D_{\max} - D_{\min}}{2}\right) \tanh(Z). \tag{10}$$

In the local theory, the relation $N(Z, g) = 0$ holds, which gives rise to the possibility of the L-H bifurcation shown in Fig. 4. Setting $\epsilon = 0$, Eqs. (7) and (8) lead to a Ginzburg-Landau equation which is solved numerically for appropriate boundary conditions, say $d(\ln(n))/dx = -1/\lambda_s$ at the edge and fixed particle flux Γ_{in} from the core. Periodic solutions for edge density and loss flux Γ_{out} are found in a restricted parameter range near the L-H transition condition and the behavior of Γ_{out} resembles the D_α emission during ELMs shown in Fig. 5. The parameter space for the occurrence of these limit cycle is

$$D_m/g_m < \Gamma_{in}\lambda_s^2 < D_M/g_M \tag{11}$$

where $g_{m,M} = g_0 \mp 2\beta(\alpha/3\beta)^{3/2}$ and $D_{m,M} = D(Z = \pm\sqrt{\alpha/3\beta})$.

During the cycle a transport barrier in D is produced near the edge as n rises, D having a smooth variation, due to the viscosity μ, over a width $\Delta \simeq \sqrt{2\beta\mu/\alpha}$ (for small μ) in which poloidal rotation exists. The period of these oscillation is given by $\tau \simeq C\alpha\lambda_s\Delta/D_M$, where $C \sim O(1)$ is a numerical coefficient. For fixed

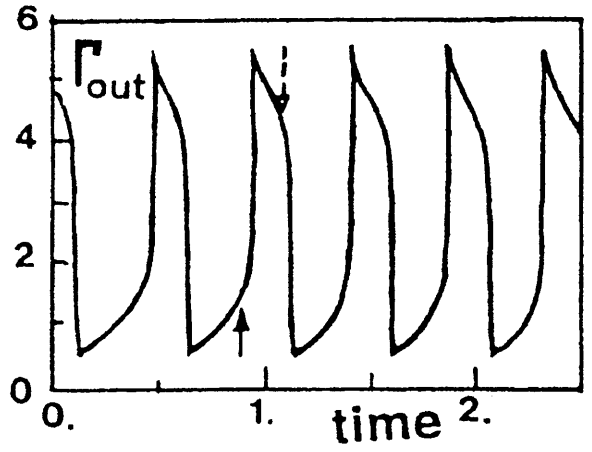

Fig. 5 Temporal evolution of the outflux Γ_{out} corresponding to the model of Fig. 4. (Cited from Ref. [22])

value of λ_s^2/D_M, the relation $\tau \propto D_M^{-0.5}$ is obtained; for fixed value of $\Gamma_{in}\lambda_s^2$, $\tau \propto \Gamma_{in}^{-0.5}$ is obtained. The ratio of τ to the period of good confinement τ_H can vary between 0 and 1. The parameters α, β, D_m, D_M can be evaluated for a specific L-H bifurcation model. Thus for the model of Ref. [21], one can set $\alpha = 3\beta = 3(1 - d\sqrt{\ln(2e/d)})/2(1 + d\sqrt{\ln(2e/d)})$, $D_m \simeq d$, $D_M \simeq d/2\ln(2e/d)$.

The earlier local L-H bifurcation model has been further extended by considering transport equation of temperature T in addition to that of density n and radial electric field Z [16]. Both diffusivity D and heat diffusivity χ have similar dependences on Z. The boundary conditions are imposed by specifying the particle flux Γ_{in} and the heat flux q_{in} from the core. The gradient lengths λ_n and λ_T at the plasma edge are applied. This system has more complicated propaties, in which increases in n drive it towards the L-mode, whereas increases in T drive it to the H-mode. This model is used to describe dithering H-modes rather than ELMs.

2.2.2 Magnetic Braiding Mode Transition

An anomalous transport theory has been developed based on the self-sustained turbulence of the current-diffusive ballooning mode (CDBM) or interchange mode (CDIM) [23], including the effect of velocity shear [24]. The CDBM model is derived by a self-consistent treatment of pressure-gradient-driven turbulence involving transport coefficients (e.g. a turbulent current diffusivity in Ohm's law) due to the same turbulence. The theory may well explain the L- and H-mode confinement characteristics (including the low/reversed shear cases) [25, 26]. In the L- and H-mode transport, the $\tilde{\boldsymbol{E}} \times \boldsymbol{B}$ vortex motions determine the anomalous transport coefficients, where $\tilde{\boldsymbol{E}}$ is the electric perturbation. These transport coefficients are characterized by the pressure gradient parameter α and the model also contains the possibility of L- to H-mode transitions through the inclusion of radial electric field shear stabilization. At saturation, anomalous electron transport coefficients, χ_e and μ_e, and those for ions, χ_i and μ_i, are of the same order and $\chi_e/\mu_e \sim \chi_i/\mu_i \sim 1$ holds where χ and μ are the turbulent thermal diffusivity and viscosity, respectively.

A modified version of the CDBM transport model provides a description of giant ELMs [13]. Since the basic model involves essentially electrostatic turbulence, all transport coefficients are expected to be comparable. However, if one considers the associated magnetic perturbation and the island overlapping, then the magnetic stochasticity can set in. A new branch of self-sustained turbulence exists in the regime of high pressure gradient [27]. The branch, called the 'M-branch', is dominated by the magnetic perturbation, $\tilde{\boldsymbol{B}}$, and is associated with magnetic braiding. In the M-mode state, the selective diffusion of electrons appears, and the ratio μ_e/μ_i is increased as $\mu_e/\mu_i \sim \chi_e/\chi_i \sim M$. The ratio M is evaluated as $M \sim \sqrt{\alpha\beta_i m_i/m_e}$ where $\alpha = -Rq^2\beta'$ is the normalized pressure gradient, and $\beta_i = v_{thi}^2/v_A^2$. The transport coefficients are enhanced by factors of

$$\chi_e^M \sim (\alpha\beta_i m_i/m_e)\chi_H \quad \chi_i^M \sim \sqrt{\alpha\beta_i m_i/m_e}\chi_H, \quad (12)$$

where χ_H is the thermal diffusivity for the H-mode. This form of χ_i agrees with the result of the scale-invariance theory by Connor [28].

When the pressure gradient exceeds a critical value, the associated small-scale magnetic islands satisfy the Chirikov condition at which the magnetic braiding takes place [29], and the electron transport is preferentially increased in comparison with the ion transport, causing the stronger turbulence. The time scale on which the turbulence level grows at the onset of the H to M bifurcation, $\hat{\tau}_{gr}$, is of the order of the poloidal Alfvén transit time defined by $\tau_{Ap} \equiv a\sqrt{\mu_0 n_i m_i}/B_p$, where B_p is poloidal magnetic field. This time scale is similar to that of strong linear ideal MHD stability. The boundary for the Chirikov criterion for the H-M transition, $\alpha = \alpha_c$, is plotted explicitly on the s-α diagram in Fig. 6. In the high-shear region, the boundary is given approximately as

$$\alpha = \alpha_c \sim \frac{s}{2}. \quad (13)$$

(The numerical coefficient 1/2 depends on radial electric field shear $\omega_{E1} = E_r'\tau_{Ap}/B$.) In the M-mode, one expects that the rapid transport leads to a reduction in α and, in turn, to a reduction in magnetic perturbations and a back transition to the H-mode occurs when island overlap ceases. The back transition condition from

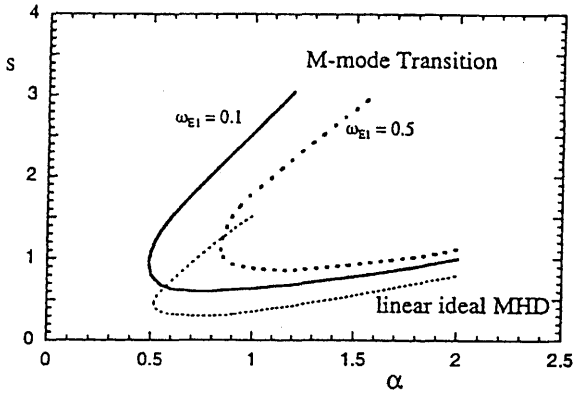

Fig. 6 The critical pressure gradient for the H-M transition in the s-α diagram form. The full curve indicates the boundary for $\omega_{E1} = 0.1$ and the dashed curve for $\omega_{E1} = 0.5$, where ω_{E1} measures radial electric field shear. The M-mode transition does not occur for the case of lower magnetic shear. The dotted curve indicates, for reference, the linear ideal ballooning mode instability threshold. (Cited from Ref. [13])

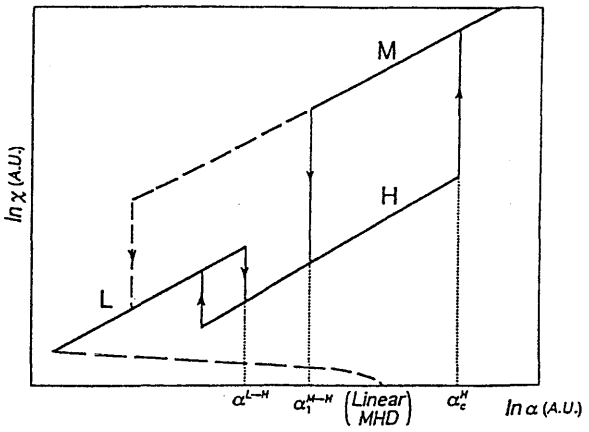

Fig. 7 Multi-fold solutions of the self-sustained turbulence, showing L, H and M phases. The thermal transport coefficient χ is shown as a function of the pressure gradient parameter α. (Cited from Ref. [13])

the M-mode to the H-mode is dictated by the M-mode characteristics. The condition is given as

$$\alpha \geq \alpha_1 \sim \sqrt{g}(1 + G\omega_{E1}^2)^{-1/4} s^{-1}. \tag{14}$$

If the pressure gradient becomes lower than α_1, a back transition to the H-mode takes place. Summarizing these bifurcation conditions, Eqs. (13) and (14), the region of multivalued branches is derived. Bistable branches of H-mode and M-mode are possible in the regime

$$\alpha_1 \leq \alpha \leq \alpha_c. \tag{15}$$

This situation leads to the bifurcation and hysteresis in the flux-gradient relation as is shown in Fig. 7. The explanation of the fast time scale is possible if this kind of transition is considered. The existence of hysteresis characteristics allows the enhanced transport in the M-mode to continue even though the free-energy source (pressure gradient, α) starts to decrease.

A cycle, involving the H-mode, the H-M transition, the M-mode and the back transition to the H-mode, is attributed to a giant ELM. A model path is considered in the following. At the critical pressure gradient, $\alpha = \alpha^{L-H}$, the plasma edge initially on the L-mode enters the H-mode phase. Since $\chi_H < \chi_L$ holds, the pressure gradient develops further. At some location r_c near the edge, the pressure gradient reaches the critical condition for the onset of the H/M transition. A sudden large loss of flux is induced. Since the relation $\chi_e^M \gg \chi_i^M$ holds, a sudden electron heat loss is initiated, followed by ion heat loss. The M-branch terminates when the plasma evacuates the excess free energy so as to reach the critical pressure gradient, α_1. Then, a back transition from the M- to H-mode occurs.

The time scale of the crash and dependence of the ELM period are discussed in Ref. [27]. Due to the enhanced heat flux of M-branch, an avalanche process can be induced. The large heat flux forces the pressure gradients at the outside and inside of first transition point r_c to increase. As a result of this increment of α, the next M-mode transition takes place at the both sides of r_c. Thus, the M-mode transition catastrophe propagates as an avalanche from r_c over a region $r_p < r < a$, with the speed

$$V_{Av} \sim l_r^M / \tau_c^M \tag{16}$$

where l_r^M and τ_c^M are the correlation length and time of the M-mode turbulence. This velocity is much faster than that due to the L-mode diffusion. The ELM period is mainly given by the heating time from $\alpha = \alpha_1^M$ to $\alpha = \alpha_c^H$. Thus the ELM frequency increases with heating power. An analytic estimate is

$$f_{ELM} \propto \frac{q^2 P}{a(a - r_p)^2 B^2} \tag{17}$$

for $P \gg P_c$, where P is the power from the plasma and P_c is the value needed to reach α_c^H. Using the thermal diffusivity from the CDBM theory one finds

$$P_c \propto B^3 / n^{3/2} \tag{18}$$

suggesting it is easier to achieve ELM-free H-modes at lower densities. For $P \geq P_c$ the dependence of f_{ELM} on

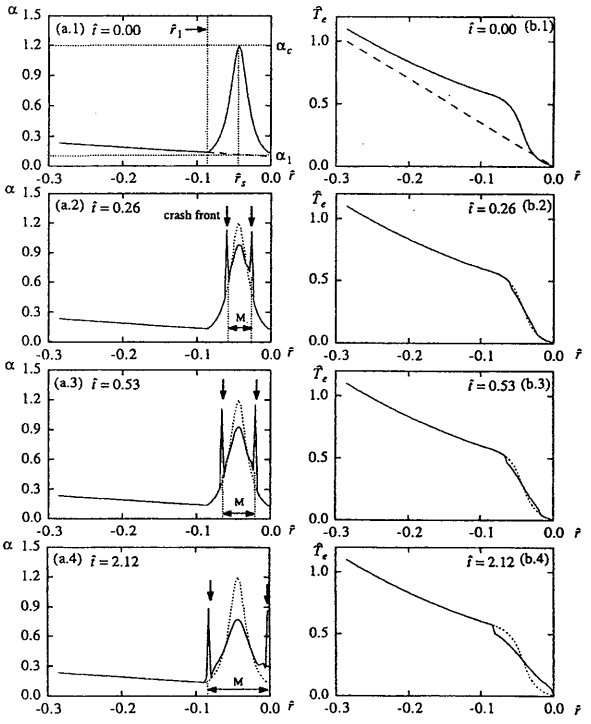

Fig. 8 The simulation of the ELM crash, taking into account the avalanche process. The time slices of the profiles of (a) the pressure gradient α and (b) the electron temperature $\hat{T}_e$ are shown from $\hat{t} = 0.00$ to 2.12, where $\hat{t} = t/\tau_{Ap}$. The numbers 1~4 corresponds to the time, $\hat{t} = 0.00$, $\hat{t} = 0.26$, $\hat{t} = 0.53$ and $\hat{t} = 2.12$, respectively. $\hat{r}_1$ is the boundary of the H-mode region, where $\hat{r} = r/a - 1$. In (a.1) and (b.1), dashed curves show the initial L-mode profiles of α and $\hat{T}_e$. In (a.2)~(a.4) and (b.2)~(b.4), the dotted curves show the initial α and $\hat{T}_e$ profiles of the H-mode at $\hat{t} = 0.00$. The arrow ↓ indicates the crash front (transition front). The transition process starts at $\hat{r}_s$. The propagation of avalanche is found. (Cited from Ref. [15])

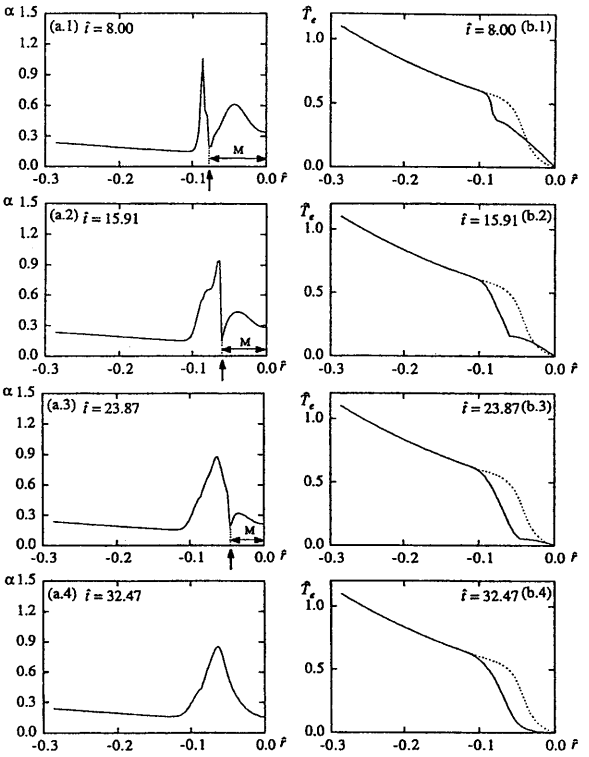

Fig. 9 The time slices of the profiles of (a) the pressure gradient α and (b) the electron temperature $\hat{T}_e$ are shown from $\hat{t} = 8.00$ to 32.47. The numbers 1~4 corresponds to the time, $\hat{t} = 8.00$, $\hat{t} = 15.91$, $\hat{t} = 23.87$ and $\hat{t} = 32.47$, respectively. In (b.1)~(b.4), the dotted curves show the initial temperature profile at $\hat{t} = 0.00$. The arrow ↑ indicates the boundary between the H-mode and the M-mode (back transition front). The erosion of profile is found. (Cited from Ref. [15])

P is modified

$$f_{ELM} \propto |\ln(P/P_c - 1)|^{-1}. \tag{19}$$

The theory also provides an estimate of the plasma energy loss δW during an ELM

$$\delta W \sim 2(1 - r_p/a)(1 - \alpha_1^M/\alpha_c^H)W_{ped} \tag{20}$$

where W_{ped} is the pedestal energy, $W_{ped} \simeq 2\pi^2 a^2 Rp(r_p)$.

A transport simulation has been performed to study the avalanche dynamics, where a model hysteresis curve for the transport coefficients is employed [14, 15]. The temporal evolutions of α and the temperature profile are shown in Fig. 8 and 9. The H-M transition is induced at the centre of the transition region, where the H-mode is established. The transition fronts propagate to both sides with a speed of order $M^2 l/\tau_{Ap}$, where l is the typical scale length. The M-mode transport and the erosion process still continue until the back transition to the H-mode is complete over the whole M-mode region. After the back transition, the edge plasma returns to the original profile on the heating time scale. The time series of the outflux and stored energy are also shown in Fig. 10. The rapid rise of outflux and the energy burst were confirmed.

An avalanche in another phenomenon is possible. A transport analysis for the high-β sawtooth crash has

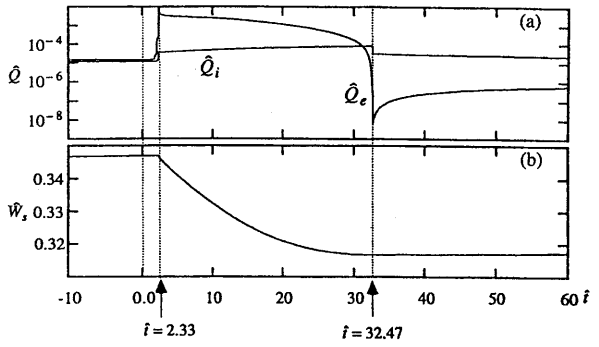

Fig. 10 The time evolutions of (a) the heat fluxes of the ion $\hat{Q}_i$ and the electron $\hat{Q}_e$ at the plasma surface and (b) the stored energy $\hat{W}_s$. The burst becomes large at around $\hat{t} = 2.33$ and terminates at $\hat{t} = 32.47$. The stored energy is exhausted by the enhanced heat flux. (Cited from Ref. [15])

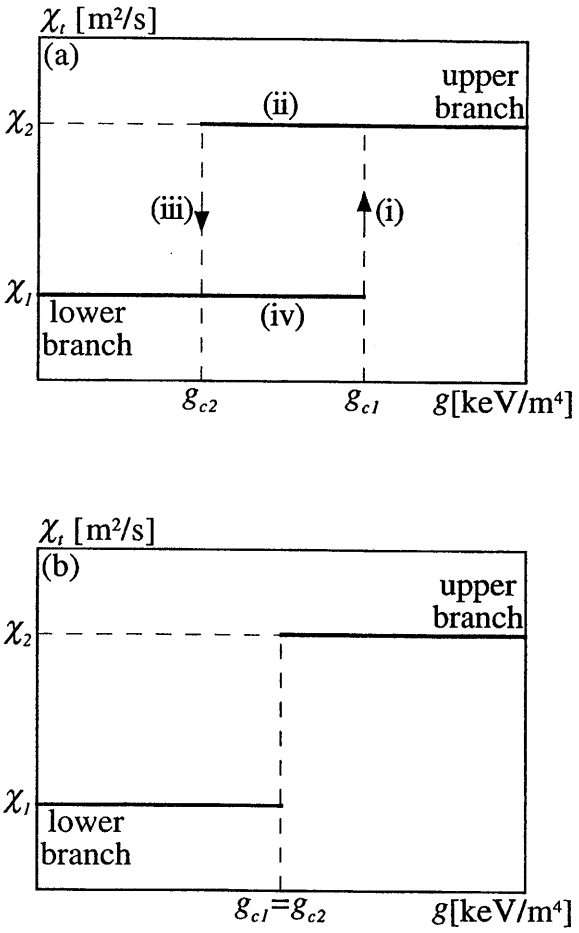

Fig. 11 The transition models of the heat diffusivity $\chi_t(g)$ (a) with hysteresis nature and (b) with discontinuity. The distance between the two thresholds is defined by $\Delta g_c \equiv g_{c1} - g_{c2}$. In the limit of $\Delta g_c \to 0$, the hysteresis nature of the model vanishes and only discontinuity remains.

also been carried out, based on the M-mode transition model [30]. The sawtooth oscillations are modeled by the repetitive transition between the L- and M-modes. The propagation of the M-mode transition front with a speed of order $M^2 l/\tau_{Ap}$ inside the $q = 1$ surface has been shown, and a crash with the fast time scale and a recovery with the slow time scale have been confirmed.

It is interesting to note the work of de Blanck in which an avalanche mechanism is applied to the problem how a localized ballooning instability can lead to a rapid propagation of its effect [31].

3. Theoretical Model for the Analysis

In this chapter, the theoretical model for the analysis is presented. The hysteresis characteristics is incorporated into the flux-force relation by introducing the transition transport model of the heat diffusivity. To examine the oscillatory characteristics of the heat transport caused by the transition model with hysteresis nature, a simplified model is introduced.

A slab geometry with Cartesian coordinates is used for the plasma edge region: $0.8 \leq x/a \leq 1$, where the main magnetic field is in the z direction, the plasma is inhomogeneous in the x direction and a is the minor radius. This region is assumed to be heated only by a constant influx from the upstream side (at $x/a = 0.8$). To clarify the characteristics of the heat transport, the density profile is assumed to be constant and uniform. As a basic equation, we employ the one dimensional (1-D) heat transport equation,

$$\frac{3}{2} n_0 \frac{\partial}{\partial t} T(x,t) = -\frac{\partial}{\partial x} q(x,t), \qquad (21)$$

where n_0, $T(x,t)$ and $q(x,t)$ are the density, the temperature and the heat flux, respectively. The heat flux is defined as

$$q(x,t) = -n_0 \chi(x,g) \frac{\partial}{\partial x} T(x,t), \qquad (22)$$

where $\chi(x,g)$ is the heat diffusivity and g represents a parameter which controls the transport. The boundary conditions are imposed as follows: a constant influx $q_{in}(t) \equiv q(0.8a,t) = const$ at the upstream side and a constant edge temperature $T(a,t) = 0$ at the downstream side.

The transition model of the diffusivity, $\chi_t(g)$, with hysteresis nature is shown in Fig. 11 (a). The absolute value of the pressure gradient is employed as a parame-

ter g,

$$g(x,t) \equiv \left| n_0 \frac{\partial}{\partial x} T(x,t) \right|. \quad (23)$$

The diffusivity has two branches. On these branches, the diffusivity is assumed to be independent of the parameter g, and is denoted by χ_1 for the lower branch and χ_2 for the upper one. The lower branch has an upper threshold of the pressure gradient, g_{c1}, and the upper branch has a lower threshold, g_{c2}. The distance between the two thresholds is defined as

$$\Delta g_c \equiv g_{c1} - g_{c2}. \quad (24)$$

In the limit of $\Delta g_c \to 0$, hysteresis nature of the model vanishes, and only discontinuity remains, as is shown in Fig. 11 (b).

The radial dependence of the diffusivity is shown in Fig. 12 (a). It is assumed to be in the following way. In the region $0.8 \leq x/a \leq 0.9$, the diffusivity is kept constant and uniform,

$$\chi(x,g) = \chi_0. \quad (25)$$

In the region $0.9 \leq x/a \leq 1$, which we call 'transition region', it has a parabolic dependence on x as,

$$\chi(x,g) = \chi_0 + (\chi_0 - \chi_t(g)) \frac{(x-0.9a)(x-a)}{((a-0.9a)/2)^2}, \quad (26)$$

where $\chi_t(g)$ is given by the transition model and takes either value of χ_1 or χ_2.

During the occurrence of the transition, the spatial region on the lower branch and that on the upper one touch each other at a location where the pressure gradient profile crosses the threshold condition. Then, the interface appears between these regions. The profile of the diffusivity on this occasion is shown in Fig. 12 (b). The interface is assumed to form the spatial 'meso-phase' where χ_t (not χ) has a linear dependence on x, and its finite thickness is denoted by δ_{meso}. These assumptions are formulated as follows: the relation,

$$\left| \frac{\partial \chi_t}{\partial x} \right| = \frac{\chi_2 - \chi_1}{\delta_{meso}}, \quad (27)$$

is assumed to hold in the region $|x - x_c| \leq \delta_{meso}/2$, where x_c represents a radial location where the threshold condition $g(x_c) = g_{c1}$ or g_{c2} is satisfied.

At a location x_c where the spatial region on the lower branch and that on the upper one touch each other, the enhanced heat flux from the region on the upper branch to that on the lower one is induced. The timescale of this 'convective transport' caused by the transition is evaluated by the convection term of eq. (21) in the meso-phase,

$$\tau_{conv} \simeq \frac{l}{|\partial \chi / \partial x|_{x=x_c}} \simeq \frac{l \delta_{meso}}{\chi_2 - \chi_1}, \quad (28)$$

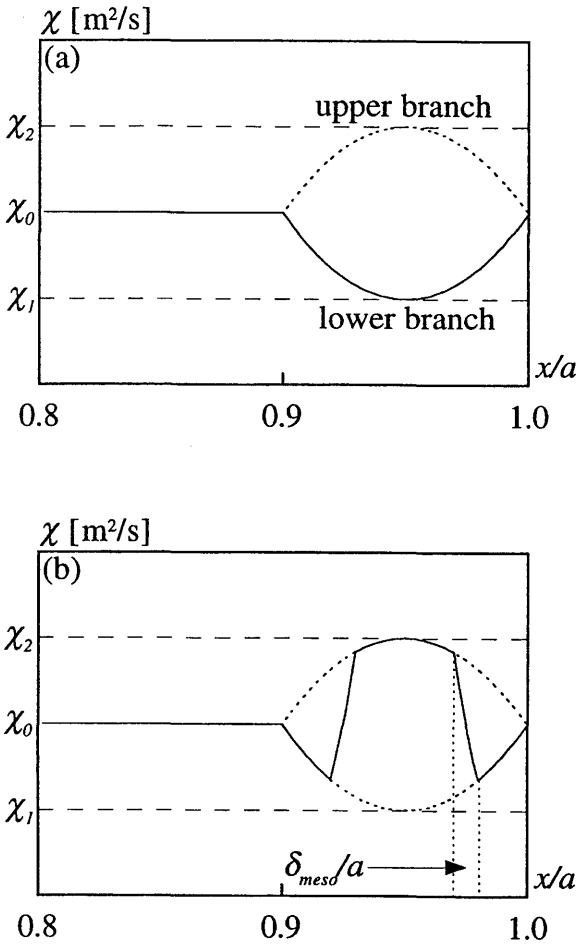

Fig. 12 The radial dependences of the heat diffusivity on the lower and the upper branch are assumed as is shown in (a). During the occurrence of the transition, the spatial region on the lower branch and that on the upper one touch each other at the location where the pressure gradient profile crosses the threshold condition. The profile of the diffusivity on this occasion is shown in (b). These two regions are assumed to be separated by the spatial 'meso-phase', and its finite thickness is denoted by δ_{meso}.

where $l = 0.1a$ is the radial length of the transition region. The system of this model has such a convection timescale in addition to the diffusive transport time scale evaluated by

$$\tau_{diff} \simeq \frac{l^2}{\chi_0}. \quad (29)$$

The parameters of a middle sized tokamak are used: $a = 0.5\text{m}$ and $n_0 = 3.0 \times 10^{19}\text{m}^{-3}$ for the plasma edge region. The values of the diffusivity are set as $\chi_0 = 1.0\text{m}^2/\text{sec}$, $\chi_1 = 0.5\text{m}^2/\text{sec}$ and $\chi_2 = 1.5\text{m}^2/\text{sec}$,

respectively. For the simplicity, the pressure gradient is normalized to g_0 as $\hat{g} = g/g_0$, where $g_0 = 10^{20}\mathrm{keV/m^4}$. One threshold is fixed at $\hat{g}_{c1} = 2.4$. Another threshold, g_{c2} $(= g_{c1} - \Delta g_c)$, is given by setting the value of Δg_c. The influx is set to $q_{in} = 1.5 \times 10^{20}\mathrm{keV/m^2sec}$ in order that the limit cycle oscillation between the two branches is possible, i.e., to satisfy the condition,

$$\chi_1 g_{c1} \leq q_{in} \leq \chi_2 g_{c2}. \tag{30}$$

The thickness of the meso-phase is assumed to be $\delta_{meso} = 5.0 \times 10^{-3}\mathrm{m}$ in order that the relation $\tau_{conv}/\tau_{diff} \sim 0.1$ may be satisfied. In other words, we consider the case that the convective transport due to the transition is much faster than the diffusive transport.

4. Simulation Study

In this chapter, based on the transition model with hysteresis nature, the heat transport in the plasma edge region is numerically analyzed from the view point of the characteristics of oscillatory behavior. In section 4.1, the time evolutions of the net loss of heat flux are simulated for three typical cases. The limit cycle processes of their oscillations are illustrated and compared with each other. The time evolutions of the pressure gradient profiles are also shown to reveal the underlying avalanche dynamics. In section 4.2, for periodic oscillation of the flux loss, the parameter dependences of its amplitude and frequency are investigated. The dependences on the influx and the distance between two thresholds are examined. In section 4.3, for irregular oscillation of the flux loss, its power spectrum is analyzed.

4.1 Time Evolution of Flux Loss

In experiments, ELM bursts are usually detected as temporal oscillations of D_α signal. Here, D_α signal represents the energy flux from the plasma surface. It corresponds to the outflux to the downstream defined by $q_{out}(t) \equiv q(a,t)$ in our model. In this section, the time evolutions of the net loss of heat flux, defined by $q_{loss}(t) \equiv q_{out}(t) - q_{in}$, are simulated for three typical values of the distance between two thresholds, (a) $\Delta\hat{g}_c = 1.2$, (b) $\Delta\hat{g}_c = 0.4$ and (c) $\Delta\hat{g}_c = 0$. The limit cycle processes of their oscillations are illustrated and compared with each other. The time evolutions of the pressure gradient profile $g(x,t)$ are also presented. The avalanche dynamics inducing the flux loss oscillations are studied.

In the case of (a) $\Delta\hat{g}_c = 1.2$, the periodic oscillation of the flux loss is observed, as is shown in Fig. 13. It consists of a limit cycle process of four steps. When the pressure gradient exceeds the threshold g_{c1}, the four steps are as follows: (i) a rapid rise of the flux loss due

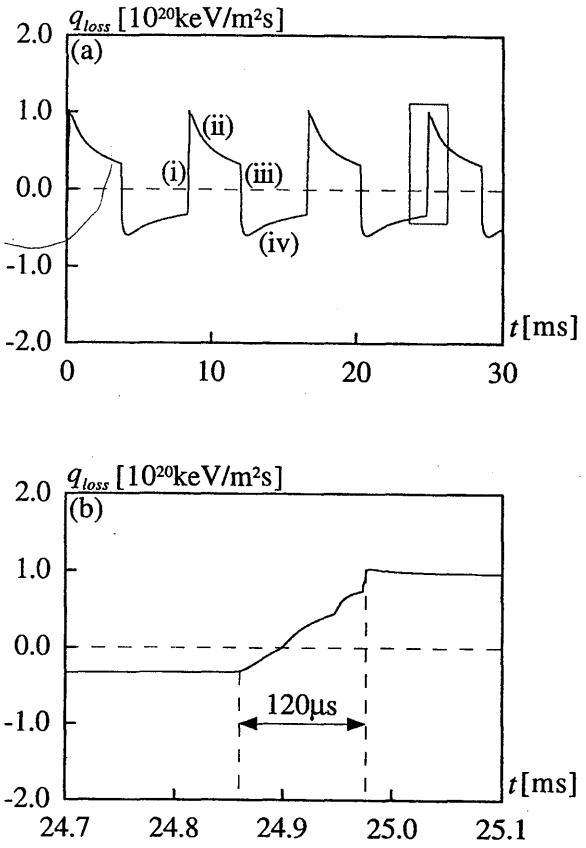

Fig. 13 (a) The time evolution of the net loss of heat flux $q_{loss}(t)$ in the case of $\Delta\hat{g}_c = 1.2$. (b) The extended view of the region surrounded by the box in (a).

to the transition from the lower to the upper branch, (ii) a gradual decrease of the flux loss in the upper branch, (iii) a sudden drop of the flux loss caused by the back transition from the upper to the lower branch and (iv) a gradual increase of the flux loss on the lower branch. These steps (i)~(iv) correspond to the states (i)~(iv) in Fig 13. The extended view of the step (i) is also shown in Fig 13 (b). The time scale of the rapid change of the flux loss in the step (i) or (iii) is in the order of convection timescale due to the transition, $\tau_{conv} = 250\mu$sec. The time scale of the gradual change in the step (ii) or (iv) are in the order of the diffusion time, $\tau_{diff} = 2.5$msec.

The corresponding pressure gradient profile, shown in Fig. 14, also repeats the periodic changes. Starting from the initial profile which just touches the threshold of the lower branch g_{c1} at the center of the transition region $x/a = 0.95$ (dotted curve), the profile repeats the cycle of four steps as follows. (i) Two pulses appear around the center of the transition region $x/a = 0.95$ and propagate making the distance

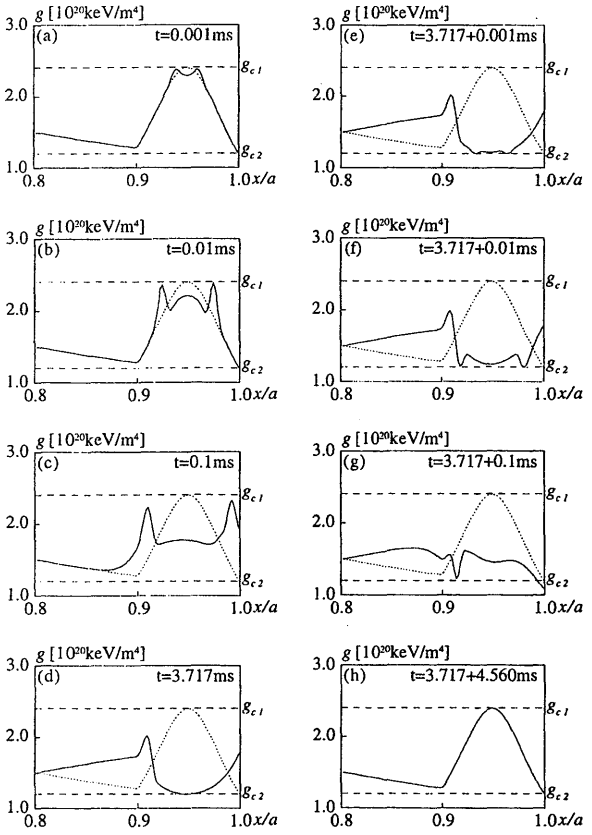

Fig. 14 The time evolution of the pressure gradient profile $g(x,t)$ in the case of $\Delta\hat{g}_c = 1.2$. The profile plotted by the dotted line in every frame shows the profile at the onset of the back transition, $t = 3.717$msec.

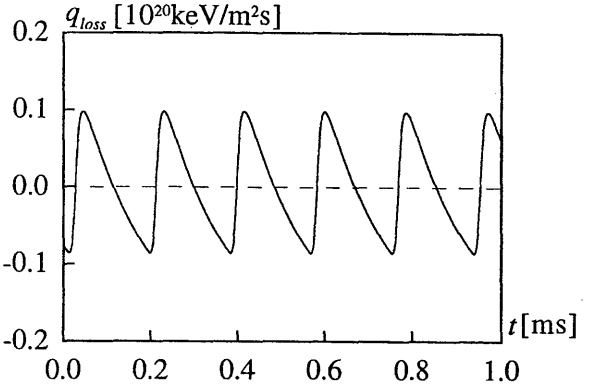

Fig. 15 The time evolution of the net loss of heat flux $q_{loss}(t)$ in the case of $\Delta\hat{g}_c = 0.4$.

between them spread by the successive transitions from the lower to the upper branch. The process is shown in Fig. 14 (i-1)~(i-3). One pulse propagates toward the upstream side, and another to the downstream side. The pulse propagating toward the upstream/downstream side in the pressure gradient profile corresponds to the cold/heat pulse in the temperature profile. The region of enhanced transport, which corresponds to that between two peaks of the pulses, expands with its propagations. In this case, the pulse to the downstream side arrives at the edge boundary and this arrival causes the rapid rise of the flux loss. (ii) The erosion of the profile is caused by the enhanced diffusivity. The profile is eroded only in the transition region and reaches the threshold g_{c2} at $x/a = 0.95$, as is shown in Fig. 14 (ii). (iii) Two negative pulses due to the back transition appear at $x/a = 0.95$ and propagate separating the distance between them by the successive back transitions from the upper to the lower branch. The process is shown in Fig. 14 (iii-1)~(iii-3). The region of the lower transport, which corresponds to that between two peaks of the negative pulses, spreads with its propagations. The negative pulse to the downstream side reaches the edge boundary to cause the sudden drop of the flux loss. (iv) The profile restores owing to the heating brought by the influx, and reaches at the threshold g_{c1} again, as is shown in Fig. 14 (iv). The time scale of the pulse propagation in the step (i) or (iii) is same as that of the rapid change of the flux loss, τ_{conv}. The time scale of the erosion in the step (ii) or the recovery in the step (iv) is in the order of the diffusion time, τ_{diff}.

Periodic bursts of the flux loss are also found in case (b) $\Delta\hat{g}_c = 0.4$, as is plotted in Fig. 15. In this case, the only rapid rise and sudden drop of the flux loss are repeated frequently. The gradual change of the flux loss is hardly observed within the one limit cycle process, since the period of the oscillation is much smaller than the diffusion time scale, $\tau \ll \tau_{diff}$, where τ is the oscillation period, i.e., the duration time of the one limit cycle process.

The corresponding time series of the pressure gradient profile at the saturated state is shown in Fig. 16. The profile change in this case is also periodic, but is mainly caused by the propagations of pulses. The limit cycle process is dominated by two steps which are the counterpart of steps (i) and (iii) in case (a). When the profile exceeds the threshold of the lower branch g_{c1}, two pulses appear and propagate just like the step (i) in the case of (a). But the pulses are ceased by the threshold g_{c2} and the pulse toward the downstream side does not reach the edge boundary. The process is shown in Fig. 16 (i-1)~(i-3). When the pulses stop their propagation, the back transition starts at the tails of the pulses. The location is indicated by arrows in Fig 16 (i-3). The negative pulses generated by the tails of the pulses propagate so as to get closer to each other, and

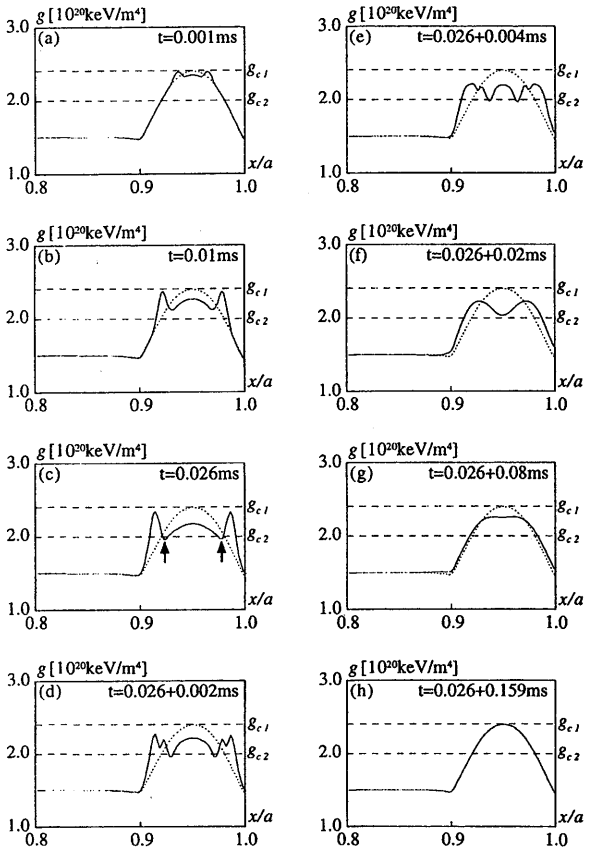

Fig. 16 The time evolution of the pressure gradient profile $g(x,t)$ in the case of $\Delta\hat{g}_c = 0.4$. The profile plotted by the dotted line in every frame shows the profile at the onset of the back transition, $t = 0.026$msec.

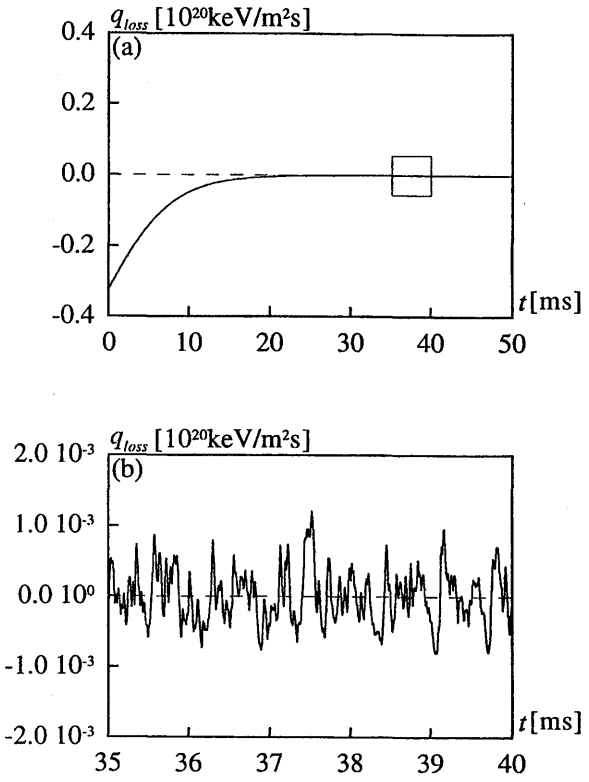

Fig. 17 (a) The time evolution of the net loss of heat flux $q_{loss}(t)$ in the case of $\Delta\hat{g}_c = 0$. (b) The extended view of the region surrounded by the box in (a).

finally merge at $x/a = 0.95$. The process is shown in Fig. 16 (ii-1)~(ii-5). The erosion and the recovery of the profile in the time scale τ_{diff} are not observed.

In case (c) $\Delta\hat{g}_c = 0$, shown in Fig. 17 (a), the flux loss approaches to the steady state value, namely, $q_{loss}(t) = 0$. But, it is accompanied by the extremely small component of irregular fluctuations. The zoomed view is also shown in Fig. 17 (b). These fluctuations are caused by repetitions of forward transitions and back transitions at the discontinuous point of $\chi_t(g)$. The periodic oscillation observed in case (a) and (b) is not revealed.

The pressure gradient profiles at the initial and the final saturated state are shown in Fig. 18. The pressure gradient hardly exceeds the threshold $g_{c1} = g_{c2}$ and the steady state profile has the flattened region reaching the threshold. In reality, the repetitive transition and back transition occur continuously in the region where the profile touches the threshold condition, so that the pressure gradient profile always fluctuates. No periodic change of the profile is observed.

4.2 Characteristics of Periodic Oscillation

In previous section 4.1, the periodic oscillations of the flux loss are observed for the finite values of Δg_c. In this section, for the periodic oscillation of the flux loss (for finite Δg_c), the parameter dependences of its amplitude and frequency are investigated. The dependences on the influx are examined in subsection 4.2.1, and those on Δg_c in subsection 4.2.2.

4.2.1 Dependences of Amplitude and Frequency on Influx

The dependence of the ELM frequency on the input power has been extensively investigated in experiments. The types of ELM bursts are generally classified with respect to the power dependence of the frequency. In our model, the heat source is given by the influx instead of the power deposition. In this subsection, the dependences of the amplitude and frequency of the flux loss on the influx are investigated. Those are simulated for the two values of finite Δg_c, (a) $\Delta\hat{g}_c = 1.2$ and (b)

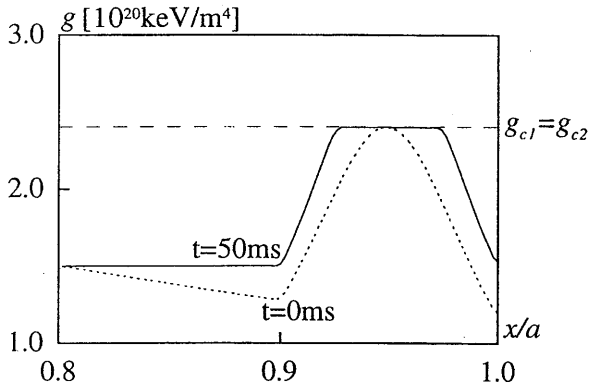

Fig. 18 The time evolution of the pressure gradient profile $g(x,t)$ in the case of $\Delta\hat{g}_c = 0$. The profile plotted by the dotted line shows the initial profile at $t = 0$msec. The solid line is the saturated state profile at $t = 50$msec.

$\Delta\hat{g}_c = 0.4$. The amplitude and the frequency are obtained from the time series of the flux loss in a saturated state, $t \gtrsim 30$msec. The amplitude, Δq_{loss}, is calculated as the difference between the minimum and maximum values of the flux loss, $\Delta q_{loss} \equiv (q_{loss}^{max} - q_{loss}^{min})/2$, where q_{loss}^{min} and q_{loss}^{max} are minimum and maximum of the flux loss, respectively. The frequency, ν, is determined as the reciprocal of the duration time of one limit cycle process, $\nu \equiv 1/\tau$.

Figure 19 shows the dependences of the amplitude (a) and the frequency (b) of the flux loss on the influx q_{in} in the case of $\Delta\hat{g}_c = 1.2$. As the influx increases, three phases appear: the stationary phase on the lower branch, the oscillatory phase with the limit cycle between two branches, and the stationary phase on the upper branch. In the oscillatory phase, the amplitude of the flux loss is almost independent of the influx. In this case, the pressure gradient pulse caused by the transition reaches the downstream side boundary in the whole region of oscillatory phase. On the other hand, the non-monotonous relation between the frequency of the flux loss and the influx is observed. The sign of $\partial\nu/\partial q_{in}$ has a reversal point near the center of the oscillatory phase. In the left region of the top of the frequency curve, the duration time staying on the lower branch τ_1 is longer than that on the upper branch τ_2. In the right region, this relation is reversed, $\tau_1 < \tau_2$. This is because larger influx makes the erosion of the profile slower and the restoration faster. Since these duration time of τ_1 and τ_2 have nonlinear dependence on the influx, such a convex form dependence of the frequency is derived from $\nu = 1/\tau = 1/(\tau_1 + \tau_2)$.

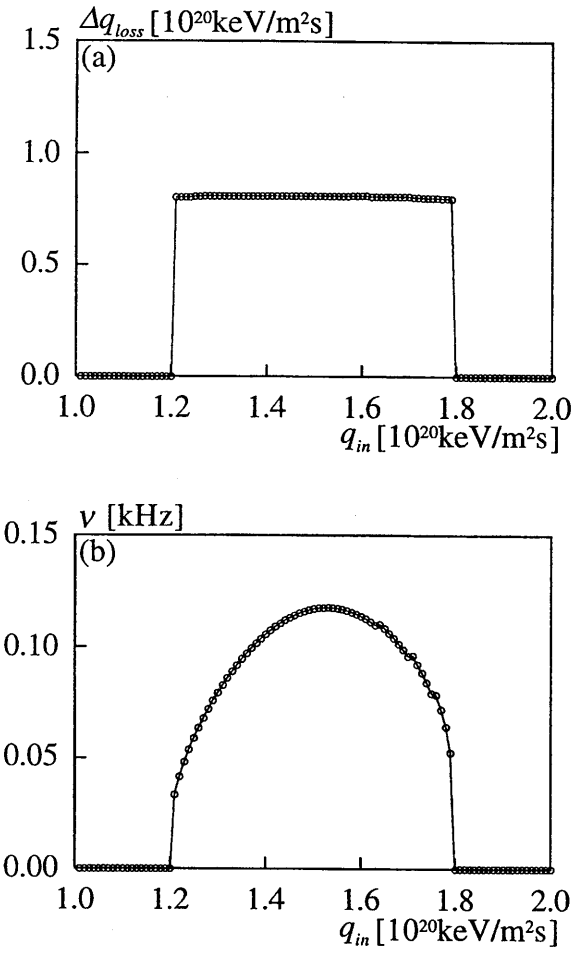

Fig. 19 The dependences of (a) the amplitude Δq_{loss} and (b) the frequency ν of the flux loss on the influx q_{in} in the case of $\Delta\hat{g}_c = 1.2$.

Figure 20 shows the dependences of the amplitude (a) and the frequency (b) of the flux loss on the influx q_{in} in the case of $\Delta\hat{g}_c = 0.4$. From the amplitude dependence in Fig 20 (a), three regions with the different types of the dependency are found in the oscillatory phase, which are divided discontinuously. In the left side region of the oscillatory phase, the amplitude and the frequency increase with the influx. Since the pressure gradient pulse caused by the transition does not arrive at the upstream side boundary in this regime, the pulse repeats to make a round trip in the transition region frequently. Therefore, the oscillation has small amplitude and high frequency. As the influx increases, the pressure gradient pulse caused by the transition becomes possible to arrive at the downstream side boundary, and the amplitude increases rapidly. Therefore, in the center region of the oscillatory phase, the avalanche

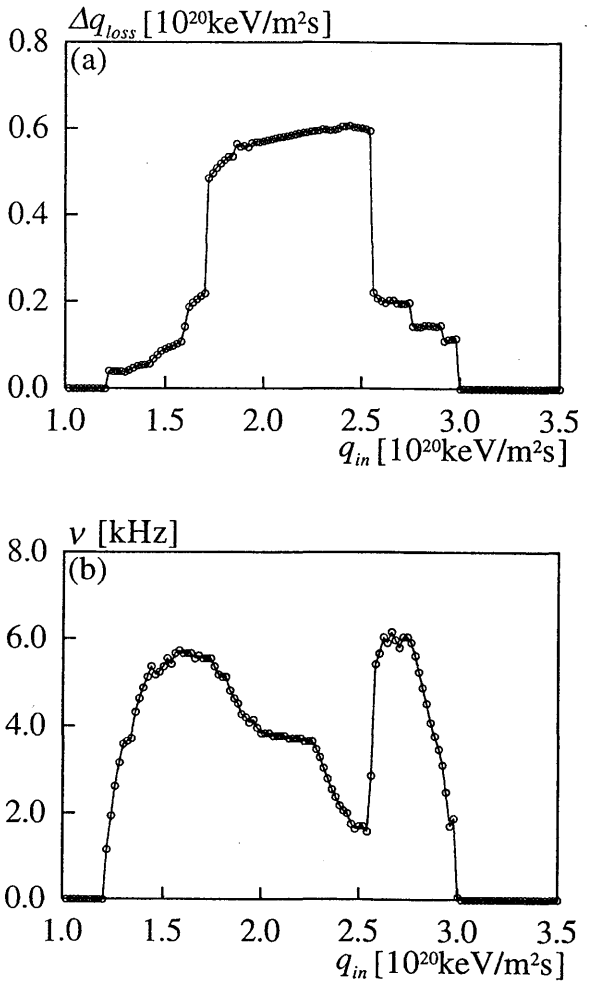

Fig. 20 The dependences of (a) the amplitude Δq_{loss} and (b) the frequency ν of the flux loss on the influx q_{in} in the case of $\Delta\hat{g}_c = 0.4$.

dynamics of pulse propagation is similar to the previous case $\Delta\hat{g}_c = 1.2$. But, the tendency that the amplitude slightly increases with the influx is different from the case of $\Delta\hat{g}_c = 1.2$. The frequency gradually decreases as the influx increases. The opposite amplitude and frequency dependences to those in the left side region are found in the right side region of the oscillatory phase. In this regime, the duration time staying on the upper branch is much longer than that on the lower branch, and the negative pulse of the pressure gradient caused by the back transition does not arrive at the upstream side boundary. The negative pulse goes up and down the transition region frequently.

Various oscillatory dependences on the influx are found in the model with hysteresis. Especially, with respect to the frequency dependences on the input power, both types of bursts, i.e., $\partial\nu/\partial P > 0$ and $\partial\nu/\partial P < 0$, are found to be possible, where P is the power input.

4.2.2 Dependences of Amplitude and Frequency on Distance Between Two Thresholds

In section 4.1, the different types of oscillatory behavior are observed for the different values of Δg_c. In this subsection, the dependences of the amplitude and frequency of the flux loss on the distance between two thresholds are investigated. Especially, it is important to analyze the behavior in the limit of $\Delta g_c \to 0$, which corresponds to the critical behavior of the transition between two transport mechanisms, i.e., the hysteresis type and the discontinuous one.

Figure 21 shows the dependences of the amplitude (a) and the frequency (b) of the flux loss on the distance between the two thresholds, Δg_c. The value of $\Delta\hat{g}_c$ is altered from 0.1 to 1.4. From Eqs. 24 and 30, the limit cycle oscillation of the flux loss occurs provided that the condition $\chi_1 g_{c1} \leq q_{in} \leq \chi_2(g_{c1} - \Delta g_c)$ holds. As Δg_c increases, the second expression of inequality becomes not to be satisfied. The limit cycle condition is violated in the regime of $\Delta\hat{g}_c > 1.4$. There, the pressure gradient is maintained above the lower threshold g_{c2} on the upper branch, and the flux loss approaches to zero without the limit cycle oscillation, therefore $\Delta q_{loss} = \nu = 0$. In the range of $0.6 \leq \Delta\hat{g}_c \leq 1.4$, the amplitudes and the frequencies of the flux loss oscillation are fitted by $\Delta q_{loss} \propto \Delta g_c{}^{1/2}$ and $\nu \propto \Delta g_c{}^{-6}$, respectively. In this range, the pressure gradient pulse caused by the transition arrives at the downstream boundary. Therefore, the oscillation of the flux loss has a large amplitude and a low frequency. A change in the Δg_c dependence is found at $\Delta\hat{g}_c = 0.6$. In the range of $0 < \Delta\hat{g}_c \leq 0.6$, the scaling relations $\Delta q_{loss} \propto \Delta g_c{}^3$ and $\nu \propto \Delta g_c{}^{-3/2}$ are observed. In this range, the oscillation with small amplitude and high frequency is realized, since the pressure gradient pulse due to the transition does not reach the downstream boundary.

To check the availability of these power law relations, the further simulations are carried out for the other values of the threshold of the lower branch. The value of $\hat{g}_{c1}$ is changed as 2.2, 2.6 and 2.8. The common power law relations are obtained for different values of g_{c1}, which is shown in Fig. 22. The power law relations in the range of $0 < \Delta\hat{g}_c \leq 0.6$ can be exterpolated in the limit of $\Delta g_c \to 0$. Thus, the critical behavior of the transition between two transport mechanisms, i.e., the hysteresis type and the discontinuous one, is expected to obey the same power law relations.

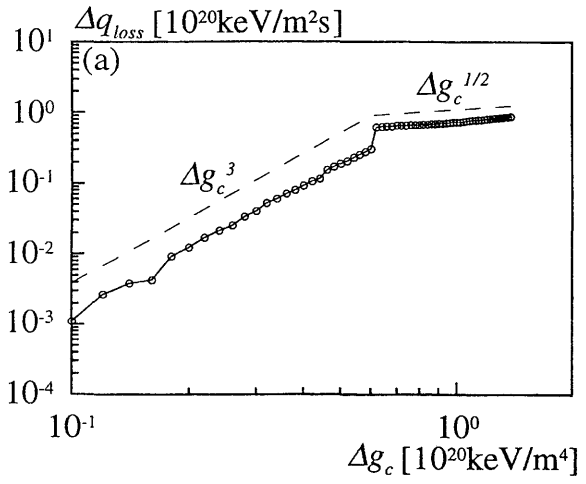

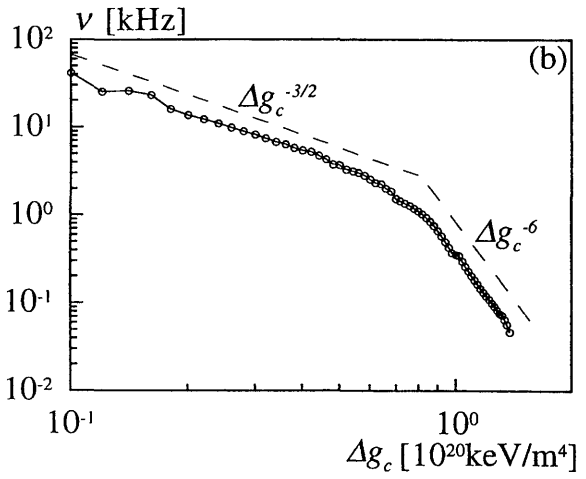

Fig. 21 The dependences of (a) the amplitude Δq_{loss} and (b) the frequency ν of the flux loss on the distance between the two thresholds Δg_c.

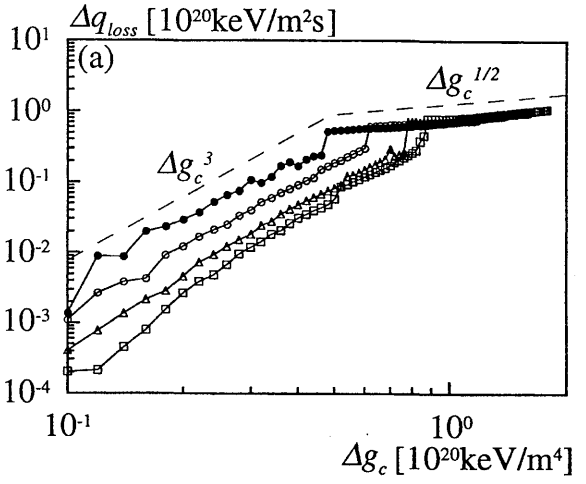

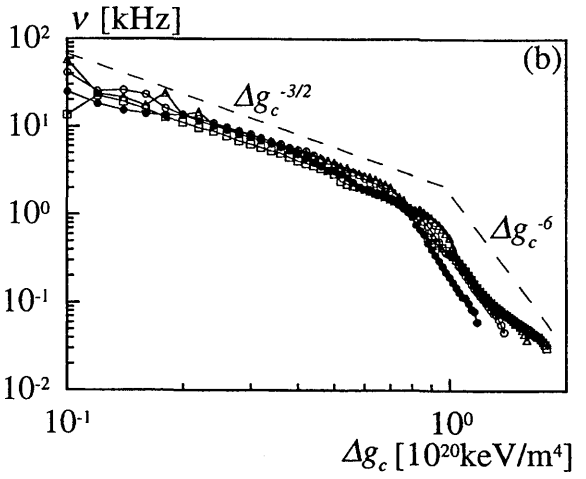

Fig. 22 The dependences of (a) the amplitude Δq_{loss} and (b) the frequency ν on the distance between the two thresholds Δg_c for several values of g_{c1}. The points •, ○, △ and □ correspond to the case of $\hat{g}_{c1}$ = 2.2, 2.4, 2.6 and 2.8, respectively.

4.3 Spectral Analysis for Irregular Fluctuation

In section 4.1, an irregular fluctuating component of the flux loss is found in the case of $\Delta\hat{g}_c = 0$, as is shown in Fig. 17. This fluctuation has small but finite amplitude. However, in previous subsection 4.2.2, the relations $\Delta q_{loss} \propto \Delta g_c{}^{7/2}$ and $\nu \propto \Delta g_c{}^{-3/2}$ are found to hold in the limit of $\Delta g_c \to 0$. Therefore, the amplitude and the frequency of the fluctuation are expected to be $\Delta q_{loss} \to 0$ and $\nu \to \infty$ in this limit, respectively. Furthermore, the observed fluctuation has irregularity although no probabilistic quantity is introduced in our model. In this section, the cause of these fluctuation and irregularity are investigated. The power spectrum of this irregular fluctuation is also analyzed.

To study the origin of the fluctuation and the irregularity, the values of the pressure gradient at the onset of the forward transition $g_{t1}(x)$ and the back transition $g_{t2}(x)$ are analyzed and compared with the given value of the threshold $g_{c1} = g_{c2}$. The differences between the actual transition points and the given thresholds are denoted by $\delta g_1 \equiv g_{t1} - g_{c1}$ and $\delta g_2 \equiv g_{t2} - g_{c2}$. These values are checked at the center of the transition region $x/a = 0.95$. The distance between the forward transition and the back transition points is defined as $\Delta g_t \equiv g_{t1} - g_{t2} = \delta g_1 - \delta g_2 + \Delta g_c$, and the relation $\Delta g_t = \delta g_1 - \delta g_2$ holds for $g_{c1} = g_{c2}$. The probability distribution functions (PDF) of the differences between the transition points and the threshold, $P_1(\delta g_1)$

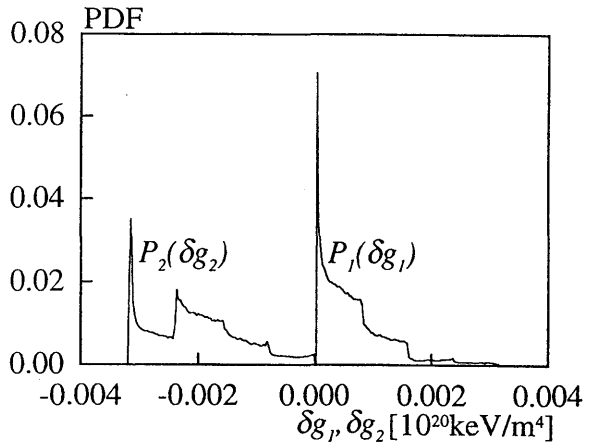

Fig. 23 The probability distribution functions of the differences between the actual transition points and the given threshold, $P_1(\delta g_1)$ for the forward transition and $P_2(\delta g_2)$ for the back transition.

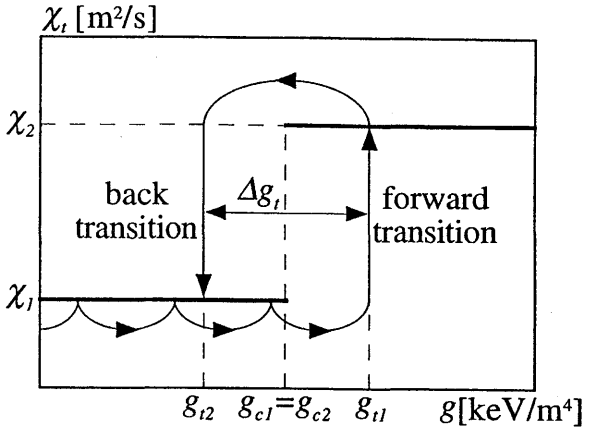

Fig. 24 The schematic illustration of the time evolution on the g-χ_t plane in the case of $\Delta \hat{g}_c = 0$.

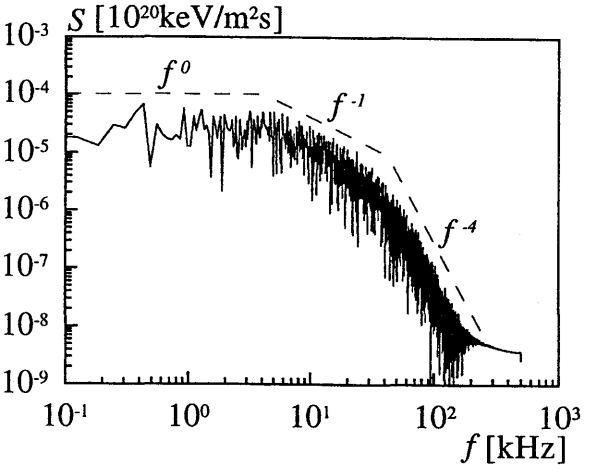

Fig. 25 The power spectrum $S(f)$ of the fluctuation in Fig. 17.

and $P_2(\delta g_2)$, are examined and shown in Fig. 23. It is found that the transition condition is probabilistic, and that the expectation value of the distance between the forward transition and the back transition points $\langle \Delta g_t \rangle$ has a finite value, where $\langle \Delta g_t \rangle \equiv \langle \delta g_1 \rangle - \langle \delta g_2 \rangle$ and $\langle \delta g_i \rangle \equiv \int \delta g_i P_i(\delta g_i) d\delta g_i$ $(i = 1, 2)$.

The actual transition point g_{t1} and back transition point g_{t2} do not strictly coincide with the given threshold condition $g_{c1} = g_{c2}$, since the finite size of discrete time steps in computation allows the pressure gradient parameter to pass the threshold without the forward transition or back transition, as is schematically illustrated in Fig. 24. The finite time step makes $\langle \Delta g_t \rangle$ finite, since the transition and the back transition do not occur at the same time step. In other words, a hysteresis with finite width $\langle \Delta g_t \rangle$ is formed by the finite size of time step. This finite $\langle \Delta g_t \rangle$ makes the flux loss fluctuate although we set $\Delta g_c = 0$. The step length of the pressure gradient evolution on the lower branch is different from that on the upper branch. By this, the iteration of limit cycle makes the orbit of the pressure gradient evolution deviate from the past one. Therefore, the actual transition point has a probability distribution. This probabilistic transition condition generates irregularity. Note that this probabilistic transition condition always exists, but it hardly influence the dynamics in the larger Δg_c case, i.e., $\Delta g_c / \langle \Delta g_t \rangle \simeq 1$.

The probabilistic transition condition and the finite $\langle \Delta g_t \rangle$ in our model seem to correspond to a noise and a finite size effect in the sand pile model (SPM) which shows the self-organized criticality (SOC) [32, 33, 34].

The SOC is characterized by the power spectrum of power law called '$1/f$ noise'. The power spectrum $S(f)$ of the irregular fluctuating component in Fig. 17 (b) is shown in Fig. 25. The power spectrum is defined by $S(f) = \sqrt{|\tilde{q}_{loss}(f)|^2}$, where $\tilde{q}_{loss}(f)$ is the Fourier component of $q_{loss}(t)$ and is complex. The power law dependences of the power spectrum are found. Following the works of Refs. [35, 36], the spectrum can be divided into three characteristic regions as follows. In the high frequency end of the spectrum, $50 \leq f$[kHz] ≤ 200, the dependence $S \propto f^{-4}$ is obtained. This frequency band is identified as the noninteracting event region. The enhanced fluxes caused by the transition do not overlap with each other and are isolated events. In the middle

frequency range, $5 \leq f[\mathrm{kHz}] \leq 50$, the spectrum is fitted as $S \propto f^{-1}$. The local events may overlap with each other in this region, and a large avalanche can be formed by their coalescence. The $1/f$ spectrum is indicative of the lack of characteristic scale for the avalanche. In the low frequency range, $0.1 \leq f[\mathrm{kHz}] \leq 5$, the spectral power becomes flat, $S \propto f^0$. This region is considered as the cutoff of $1/f$ dependence by the finite system size restriction. The events in this region are global discharge events with the scale of spatial spread comparable with the system size. These three spectral regions have been identified in the SPM and they are the characteristics of many SOC systems. These scaling relations of the power spectrum are also obtained for finite but small values of Δg_c. The SOC-like behavior is expected to appear under the condition $\Delta g_c/\langle \Delta g_t \rangle \lesssim 0.9$.

5. Summary and Discussion

In this paper, we studied edge relaxation phenomena observed in high temperature plasmas from the view point of the oscillatory characteristics of the heat transport. The oscillatory behavior of the heat transport in the plasma edge region was investigated by an approach based on nonlinear transport with limit cycle solution. The hysteresis type flux-force relation was incorporated into the model by introducing the transition transport model of heat diffusivity with hysteresis nature. Based on the model, we numerically analyzed the time evolution of heat flux and the parameter dependences of its amplitude and frequency. A part of our analysis with respect to the parameter dependence has been reported in Ref. [37].

In chapter 2., the empirical phenomenology of ELM was reviewed. The experimental classifications of ELMs were presented. The theoretical models of ELMs were also reviewed. Especially, we reviewed two transition models with hysteresis nature, i.e., the electric field bifurcation theory and the magnetic braiding mode transition model.

In chapter 3., the theoretical model for the present analysis was introduced. Based on the 1-D heat transport equation, the heat transport in the plasma edge region heated only by a constant influx from the upstream side was considered. The hysteresis characteristics were incorporated in the flux-force relation by introducing the transition transport model of heat diffusivity with hysteresis nature. To investigate the characteristics of oscillatory behavior caused by the hysteresis nature, a simplified transition model was introduced.

In chapter 4., based on the transition model with hysteresis nature, the oscillatory behavior of the net loss of heat flux was investigated.

First, we analyzed the time evolutions of the net loss of heat flux. The underlying avalanche dynamics were studied showing the time evolution of the pressure gradient profile. For finite values of hysteresis width with respect to the pressure gradient Δg_c, the periodic process of the limit cycle oscillation exists. Two typical cases with finite Δg_c were shown to have different types of the periodic oscillations depending on whether the pulse of the pressure gradient generated by the transition arrives at the edge boundary or do not. If the pulse reaches the boundary, the flux loss repeated the limit cycle process of four distinct steps, i.e., rapid rise by the transition, gradual decrease due to the erosion of the profile, sudden drop by the back transition and gradual increase by the recovery of the profile. In the case without an arrival of the pulse at the boundary, only rapid rise and sudden drop of the flux loss were repeated. This oscillation has the small amplitude and the high frequency compared with the case of the pulse arriving at the boundary. For $\Delta g_c = 0$, the profile hardly develops to excess the threshold and approaches to the steady state profile. The flux loss gets close to the steady value, but is accompanied with the small component of the irregular fluctuations due to the limit cycle oscillation around the discontinuous point of the diffusivity. This fluctuation is found to be generated by the probabilistic transition condition and the finite size effect of the pressure gradient owing to the discrete time steps in computation. The situation of transport in this case was very similar to the evolution rule of SPM, and the power spectrum which obeys power law relations is obtained.

Second, the parameter dependences of the amplitude and the frequency of the flux loss were investigated. The amplitude has weak or no dependence on the influx when the positive or negative pulse of the pressure gradient reaches the downstream boundary. While, in the case without the arrival of the pulse at the boundary, it has dependence. The non-monotonous dependences of the frequency on the influx were observed for given values of Δg_c. With respect to the dependences on the distance between two thresholds, the amplitude and frequency were fitted by $\Delta q_{loss} \propto {\Delta g_c}^{1/2}$ and $\nu \propto {\Delta g_c}^{-6}$, respectively, in the region of $0.6 \leq \Delta \hat{g}_c \leq 1.4$. The limit of $\Delta g_c \to 0$ was investigated, and the transition between two transport mechanisms, i.e., the hysteresis type and the discontinuous one, was clarified. Power law relations of the amplitude, $\Delta q_{loss} \propto {\Delta g_c}^3$, and the frequency, $\nu \propto {\Delta g_c}^{-3/2}$, were obtained for $0 < \Delta \hat{g}_c \leq 0.6$. Analyzing such change of the oscillatory characteristics may give a key to understand the mechanism of the collapse.

For future work, we investigate the influence of the meso-phase thickness on the oscillatory characteristics of the flux loss. For periodic oscillation (for finite Δg_c),

the dependences of the amplitude and frequency of the flux loss on the meso-phase thickness is analyzed. The timescale of the convection due to the transition is determined by the thickness of meso-phase according to Eq. 27. Therefore, the smaller Δg_c case, in which the period of the oscillation is in the order of convection timescale, is expected to be much more strongly affected by the change of δ_{meso}. For irregular oscillation, which corresponds to the smallest Δg_c case, i.e., $\Delta g_c = 0$, the influence of the moso-phase thickness on the power spectrum can be examined. The coalescence of neighboring local events due to the transition is promoted by the overlap of their meso-phases. Therefore, the wider δ_{meso} makes the probability of large event occurrence be higher. The large amplitude (or low frequency) component of power spectrum is expected to increase. The characteristics of SOC-like behavior will be further analyzed with well-defined origin of irregular fluctuation. For finite Δg_c case, a probabilistic component is introduced in the influx (or the thresholds). Then, the irregular fluctuation may be caused by the finite size effect due to given Δg_c and the incorporated noise instead of the finite size effect and the noise due to the discrete time step in computation. These are left for our future work.

Acknowledgment

The authors thank Professor K. Itoh for many useful suggestions. This work is partly supported by the Grant-in-Aid for Scientific Research of the Ministry of Education, Science, Sport and Culture in Japan and by collaboration programme of Advanced Fusion Research Center/RIAM of Kyushu University.

References

1) Itoh, S.-I., Itoh, K., Zushi, H. and Fukuyama, A.: *Plasma Phys. Control. Fusion*, Vol.40, (1998) 879

2) Artsimovich, L.A.: *Nucl. Fusion*, Vol.12, (1972) 215

3) von Goeler, S., Stodiek, W. and Sauthoff, N.: *Phys. Rev. Lett.*, Vol.33, (1974) 1201

4) Koide, Y., *et al.*: *Phys. Rev. Lett.*, Vol.72, (1994) 3662

5) Taylor, T.S., *et al.*: *Plasma Physics and Controlled Nuclear Fusion Research (Vienna: IAEA)*, Vol.1, (1984) 421

6) Zohm, H.: *Plasma Phys. Control. Fusion*, Vol.38, (1996) 105

7) Keilhacker, M., Becker, G., Bernhadi, K., *et al.*: *Plasma Phys. Control. Fusion*, Vol.26, (1984) 49

8) Doyle, E.J., *et al.*: *Phys. Fluids B*, Vol.3, (1991) 2300

9) Connor, J.W.: *Plasma Phys. Control. Fusion*, Vol.40, (1998) 191

10) Itoh, S.-I., Itoh, K. and Fukuyama, A.: *Nucl. Fusion*, Vol.33, (1993) 1445

11) ASDEX team: *Nucl. Fusion*, Vol.29, (1989) 1959

12) Gohil, P., *et al.*: *Phys. Rev. Lett.*, Vol.61, (1988) 1603

13) Itoh, S.-I., Itoh, K., Fukuyama, A. and Yagi, M.: *Plasma Phys. Control. Fusion*, Vol.38, (1996) 527

14) Kubota, T., Iwasaki, T., Itoh, S.-I., *et al.*: *Proc. 24th Eur. Conf. on Controlled Fusion and Plasma Physics (Berchtesgaden) Europhys. (Geneva: EPS)*, Vol.21A part.IV, (1997) 1769

15) Kubota, T., Itoh, S.-I. and Yagi, M.: *J. Phys. Soc. Jpn.*, Vol.67, (1998) 3100

16) Zohm, H.: *Phys. Rev. Lett.*, Vol.72, (1994) 222

17) Zohm, H., Büchl, K., Field, A.R., Fucks, J.C., Gehre, O., Herrmann, A., Kaufmann, M., Lieder, G., Ryter, F., Schittenhelm, M., ASDEX-Upgrade Team and ICRF-Group: *Proc. 20th Eur. Conf. on Controlled Fusion and Plasma Physics (Lisbon) Europhys. (Geneva: EPS)*, Vol.17 part.I, (1993) 23

18) DIII-D team: *Plasma Physics and Controlled Nuclear Fusion Research (Proc. 13th Int. Conf. (Washington DC, 1990)) (Vienna: IAEA)*, Vol.1, (1991) 629

19) Osborne, T.H., Burrel, K.H., Carlstrom, T., *et al.*: *Bull. Am. Phys. Soc.*, Vol.35, (1990) 1975

20) Huysmans, G.T.A., Challis, C.D., Erba, M., Kerner, W. and Parail, V.V.: *Proc. 22nd Eur. Conf. on Controlled Fusion and Plasma Physics (Bournemouth) Europhys. (Geneva: EPS)*, part.I, (1995) 201

21) Itoh, S.-I. and Itoh, K.: *Phys. Rev. Lett.*, Vol.60, (1988) 2276

22) Itoh, S.-I., Itoh, K., Fukuyama, A., Miura, Y. and JFT-2M Group: *Phys. Rev. Lett.*, Vol.67, (1996) 2485

23) Itoh, K., Itoh, S.-I. and Fukuyama, A.: *Phys. Rev. Lett.*, Vol.69, (1992) 1050

24) Itoh, S.-I., Itoh, K., Fukuyama, A. and Yagi, M.: *Phys. Rev. Lett.*, Vol.72, (1994) 1200

25) Fukuyama, A., Itoh, K., Itoh, S.-I., Yagi, M. and Azumi, M.: *Plasma Phys. Control. Fusion*, Vol.36, (1994) 1385

26) Fukuyama, A., Itoh, K., Itoh, S.-I., Yagi, M. and Azumi, M.: *Plasma Phys. Control. Fusion*, Vol.37, (1995) 611

27) Itoh, S.-I., Itoh, K., Fukuyama, A. and Yagi, M.: *Phys. Rev. Lett.*, Vol.76, (1996) 920

28) Connor, J.W.: *Plasma Phys. Control. Fusion*,Vol.35, (1993) 757

29) Krommes, J.A. *et al.*: *J. Plasma Phys.*, Vol.30, (1983) 11

30) Kubota, T., Itoh, S.-I. and Yagi, M.: *Plasma Phys. Control. Fusion*, Vol.39, (1997) 1397

31) de Blanck, H.: Local stability criteria and burst like instabilities, *Programme and Abstracts of the 6th Eur. Theory Conf. (Utrecht, 1995) (Rijnhuizen: Instituut voor Plasmafysica)*, (1995) abstract C9

32) Dendy, R.O. and Helander, P.: *Plasma Phys. Control. Fusion*, Vol.39, (1997) 1947

33) Bak, P., Tang, C. and Wiesenfeld, K.: *Phys. Rev. A*, Vol.38, (1988) 364

34) Tang, C. and Bak, P.: *J. Stat. Phys.*, Vol.51, (1988) 797

35) Hwa, T. and Kardar, M.: *Phys. Rev. A*, Vol.45, (1992) 7002

36) Carreras, B.A., Newmann, D., Lynch, V.E. and Diamond, P.H.: *Phys. Plasmas*, Vol.3, (1996) 2903

37) Matsukawa, S., Itoh, S.-I. and Yagi, M.: Model Analysis of Edge Relaxation Phenomena, *Contrib. Plasma Phys.*, (2000) to be published

Appendix

A1. Transition Model with Discontinuous Derivative

The transition model with discontinuous derivative, shown in Fig. A1, is also considered as one of transition transport mechanisms in addition to the model with hysteresis nature and that with discontinuity shown in Fig. 11. The transition model with discontinuity and that with discontinuous derivative correspond to the phase transition of the first and second order, respectively. Here, we simulate the time evolution using the transition model of the diffusivity with discontinuous derivative.

The simplified transition model with discontinuous derivative is shown in Fig. A1. The diffusivity has an intermediate branch between the upper and the lower branch (in the region $g_{c1} \leq \Delta g_c \leq g_{c2}$) and is assumed to be a linear function of the pressure gradient on this branch. The other setup for simulation is the same as that in chapter 3., and the case of $\Delta g_c < 0$ represents the model with discontinuous derivative according to the previous definition of the thresholds.

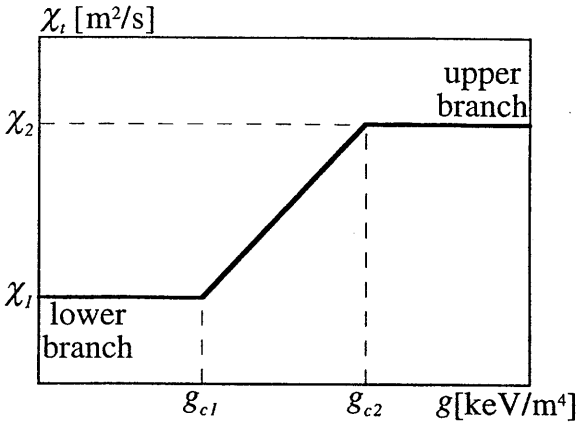

Fig. A1 The transition model of the diffusivity $\chi_t(g)$ with the discontinuous derivative.

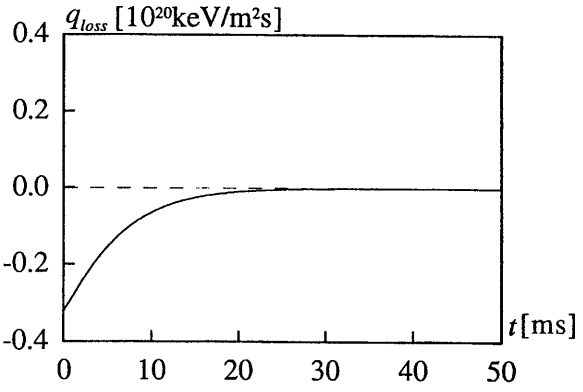

Fig. A2 The time evolution of the net loss of heat flux $q_{loss}(t)$ in the case of $\Delta\hat{g}_c = -1.2$.

The time evolution of the flux loss in the case of $\Delta\hat{g}_c = -1.2$ is shown in Fig. A2. The flux loss settles down to the steady state value, $q_{loss}(t) = 0$. The saturation of the flux loss occurs in the order of diffusion time τ_{diff}. The corresponding initial and saturated pressure gradient profiles are shown in Fig. A3. Starting from the initial profile which just comes close to the threshold of the lower branch g_{c1} at the center of the transition region $x/a = 0.95$ (dotted line), the profile partially exceeds the threshold and reaches the steady state (solid line) where the diffusion and the influx are balanced. In this case, the profile can maintain itself beyond the threshold of the lower branch.

Neither the repetitive limit cycle process nor the rapid change in the time scale τ_{conv} is found. The transition model with discontinuous derivative, which approaches the final state, belongs to the soft-type transition. The soft-type mechanism causes the gradual

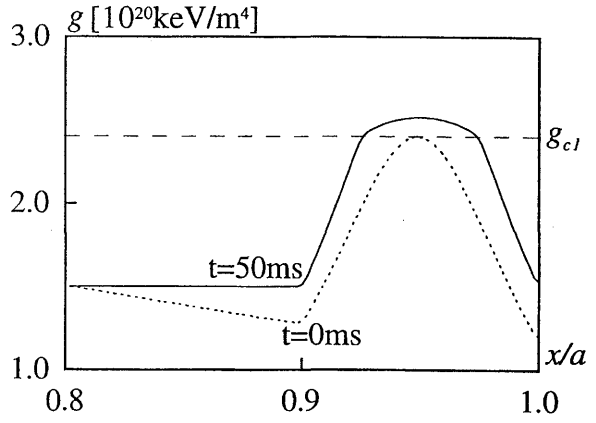

Fig. A3 The time evolution of the pressure gradient profile $g(x,t)$ in the case of $\Delta\hat{g}_c = -1.2$. The profile plotted by the dotted line shows the initial profile at $t = 0$msec. The solid line is the saturated state profile at $t = 50$msec.

transition in slow transport timescale. On the other hand, the transition models with hysteresis nature and with discontinuity, which cause the dynamic process, are categorized in the hard-type transition. The hard-type mechanisms cause the sudden transition in fast convection timescale. Moreover, work-done to the outside of system is realized by hysteresis nature. A hysteresis nature has a potentiality to explain the fast growth of the outward heat flux and the evacuation of the plasma energy induce by ELMs.